Space Weather

RESEARCH ARTICLE
10.1029/2019SW002217

Solar Wind Properties and Geospace Impact of Coronal Mass Ejection-Driven Sheath Regions: Variation and Driver Dependence

E. K. J. Kilpua[1], D. Fontaine[2], C. Moissard[2], M. Ala-Lahti[1], E. Palmerio[1], E. Yordanova[3], S. W. Good[1], M. M. H. Kalliokoski[1], E. Lumme[1], A. Osmane[1], M. Palmroth[1], and L. Turc[1]

[1]Department of Physics, University of Helsinki, Helsinki, Finland, [2]Laboratoire de Physique des Plasmas, Ecole polytechnique, CNRS, Sorbonne Université, Université Paris-Sud, Observatoire de Paris, Université Paris-Saclay, PSL Research University, Palaiseau, France, [3]Swedish Institute of Space Physics, Uppsala, Sweden

Abstract We present a statistical study of interplanetary conditions and geospace response to 89 coronal mass ejection-driven sheaths observed during Solar Cycles 23 and 24. We investigate in particular the dependencies on the driver properties and variations across the sheath. We find that the ejecta speed principally controls the sheath geoeffectiveness and shows the highest correlations with sheath parameters, in particular in the region closest to the shock. Sheaths of fast ejecta have on average high solar wind speeds, magnetic (B) field magnitudes, and fluctuations, and they generate efficiently strong out-of-ecliptic fields. Slow-ejecta sheaths are considerably slower and have weaker fields and field fluctuations, and therefore they cause primarily moderate geospace activity. Sheaths of weak and strong B field ejecta have distinct properties, but differences in their geoeffectiveness are less drastic. Sheaths of fast and strong ejecta push the subsolar magnetopause significantly earthward, often even beyond geostationary orbit. Slow-ejecta sheaths also compress the magnetopause significantly due to their large densities that are likely a result of their relatively long propagation times and source near the streamer belt. We find the regions near the shock and ejecta leading edge to be the most geoeffective parts of the sheath. These regions are also associated with the largest B field magnitudes, out-of-ecliptic fields, and field fluctuations as well as largest speeds and densities. The variations, however, depend on driver properties. Forecasting sheath properties is challenging due to their variable nature, but the dependence on ejecta properties determined in this work could help to estimate sheath geoeffectiveness through remote-sensing coronal mass ejection observations.

Key Points:
- Variation of interplanetary properties and geoeffectiveness of CME-driven sheaths and their dependence on the ejecta properties are determined
- Ejecta speed primarily controls the sheath geoeffectiveness and correlates best with sheath parameters
- Strongest space weather response is expected during the front and end parts of the sheath

Supporting Information:
- Supporting Information S1

Correspondence to:
E. K. J. Kilpua,
emilia.kilpua@helsinki.fi

Citation:
Kilpua, E. K. J., Fontaine, D., Moissard, C., Ala-Lahti, M., Palmerio, E., Yordanova, E. et al. (2019). Solar wind properties and geospace impact of coronal mass ejection-driven sheath regions: Variation and driver dependence. *Space Weather*, *17*, 1257–1280. https://doi.org/10.1029/2019SW002217

Received 3 APR 2019
Accepted 28 JUN 2019
Accepted article online 27 JUL 2019
Published online 19 AUG 2019

©2019. American Geophysical Union. All Rights Reserved.

1. Introduction

Coronal mass ejections (CMEs; e.g., Webb & Howard, 2012) are the primary drivers of intense magnetospheric storms at Earth (e.g., Gosling et al., 1991; Huttunen et al., 2005; Richardson & Cane, 2012; Zhang et al., 2007). In interplanetary space, there are two principal large-scale structures associated with CMEs that can cause significant space weather disturbances (e.g., Kilpua, Koskinen et al., 2017). The first is the *ejecta*, which is a magnetized plasma cloud launched from the Sun and which constitutes the main part of the CME. The current consensus is that CME plasma clouds intrinsically have a magnetic flux rope (FR) configuration (Green et al., 2018; Vourlidas et al., 2013, 2017), although a clear FR structure, known also as a magnetic cloud (e.g., Burlaga, 1988; Burlaga et al., 1981; Klein & Burlaga, 1982), is not always unambiguously observed in situ due to deformations and interactions during propagation and large crossing distances of the spacecraft from the FR center (Cane et al., 1997; Cane & Richardson, 2003; Jian et al., 2006; Kilpua et al., 2011). The second is the *sheath*, which is a turbulent region that forms ahead of those CME ejecta that travel faster than the preceding solar wind, disturbing and deflecting the flow ahead. If the relative speed of the ejecta and solar wind exceeds the local fast magnetosonic speed, a shock wave that compresses and heats the plasma will form. In this case, the sheath is defined as the region between the shock and the leading edge of the ejecta. As sheaths accumulate gradually over the several days it takes a CME to reach Earth, they form layered structures where plasma and magnetic field parameters can vary considerably. Shock compression of any preceding discontinuities (e.g., Kataoka, Watari et al., 2005) and field line draping about the ejecta

(Gosling & McComas, 1987; McComas et al., 1988) lead to large-amplitude field variations. In addition, as CMEs typically expand strongly after they are launched from the Sun up to heliospheric distances of about 10–15 AU (e.g., Richardson et al., 2006), the plasma and magnetic field pile up at the leading edge of the ejecta in the sheath (e.g., Kaymaz & Siscoe, 2006; Owens et al., 2017; Siscoe et al., 2007). This turbulent and variable nature makes forecasting the space weather response to CME sheaths particularly challenging (e.g., Kilpua, Koskinen et al., 2017).

While ejecta (and particularly those containing FRs) are typically associated with the largest geomagnetic storms, sheaths can also drive intense storms themselves, and many storms have contributions from both structures (e.g., Gonzalez et al., 2011; Kataoka et al., 2015; Kilpua, Balogh et al., 2017; Huttunen et al., 2005; Lugaz et al., 2016; Tsurutani et al., 1988; Zhang et al., 2007). The effect of shocks and sheaths is particularly strong in the high-latitude magnetosphere, where they cause strong auroral currents (Huttunen & Koskinen, 2004; Huttunen et al., 2002; Zhou et al., 2003) and are potential candidates for causing so-called supersubstorms (Hajra & Tsurutani, 2018; Tsurutani et al., 2015). Furthermore, sheaths are found to result in particularly large geomagnetically induced currents (Huttunen et al., 2008) as well as intense low-energy particle precipitation to the upper atmosphere that consequently affect the thermosphere neutral density response and enhance significantly nitric oxide production (Knipp et al., 2013; 2017). Sheaths also compress significantly the dayside magnetopause location earthward (e.g., Hietala et al., 2014; Kilpua, Hietala, et al., 2015; Lugaz et al., 2016), and they have distinct effects on the outer Van Allen radiation belts, typically causing deep and sustained depletion of relativistic electrons fluxes (e.g., Alves et al., 2016; Hietala et al., 2014; Kilpua, Hietala, et al., 2015; Kilpua et al., 2019; Lugaz et al., 2016; Turner et al., 2019).

Despite their evident importance in regard to geomagnetic impact, sheaths are relatively little studied when compared to ejecta. Previous studies of general sheath properties have indicated that, due to their compressed nature, sheaths commonly have much higher values of solar wind plasma parameters than the ejecta (Guo et al., 2010; Kilpua, Koskinen et al., 2017; Kilpua, Balogh et al., 2017; Mitsakou et al., 2009; Myllys et al., 2016) and higher levels of turbulence (Kilpua et al., 2013; Kilpua, Koskinen et al. 2017). In consequence, sheaths also have higher Alfvén Mach numbers and dynamic pressures (Kilpua, Koskinen et al., 2017). These characteristics make sheaths couple particularly strongly with the magnetosphere as highlighted by both observational and simulation studies (e.g., Kataoka, Fairfield et al., 2005; Kilpua, Balogh et al., 2017; Lopez et al., 2004; Myllys et al., 2016). Probability distributions of various sheath parameters and their comparison to distributions of the same parameters for ejecta, slow-fast stream interaction regions, and fast solar wind are found, for example, in Guo et al. (2010), Myllys et al. (2016), Kilpua, Koskinen, and Pulkkinen (2017), and Kilpua, Balogh, et al. (2017). In addition, several studies have performed superposed epoch analysis of interplanetary coronal mass ejections (ICMEs) that give information also on general sheath properties, for example, the Kataoka and Miyoshi (2006) study of 49 ICME-driven storms during Solar Cycle 23, years 1996–2004, and the Rodriguez et al. (2016) study of 63 magnetic clouds between 1998 and 2006.

General and established relations between sheath and CME ejecta properties could help to predict the space weather impact of sheaths. This is because information on CME properties, and in particular CME speed, is continuously available from white-light remote-sensing observations and related reconstruction techniques in the corona and heliosphere (e.g., Mierla et al., 2010; Thernisien et al., 2009; Yashiro et al., 2004). For example, Mitsakou et al. (2009) studied and compared the properties of 67 sheaths and ejecta during 2003–2006. The authors found a strong (0.801) correlation between the mean speeds in sheaths and ejecta. The corresponding correlation of the mean magnetic field magnitude and density between the sheath and the ejecta was only moderate, at 0.662 and 0.618, respectively. Owens et al. (2005) derived an empirical relation to predict the mean magnetic field magnitude in sheaths based on the observed relation between the ejecta leading edge speed and sheath magnetic field magnitude. This relation was found only for cases where the ejecta had a magnetic FR structure. Recently, Janvier et al. (2019) studied sheaths and ejecta using observations by MErcury Surface, Space ENvironment, GEochemistry, and Ranging at the orbit of Mercury, Venus Express at the orbit of Venus, and the spacecraft upstream of Earth at the Lagrange L1 point. They also found a good correlation between the ejecta and sheath speeds, but low correlation between the magnetic field magnitudes in the sheath and ejecta. Kilpua et al. (2013) analyzed ultralow frequency (ULF) fluctuations in the interplanetary magnetic field (IMF) and in dynamic pressure for 41 sheaths observed during Solar Cycle 23 using Advanced Composition Explorer (ACE) data. All sheaths were resampled to the same average duration, and a superposed epoch analysis was performed in order to investigate how fluctuations varied from the shock to the ejecta leading edge. It was found that the fluctuation power was highest just after the shock

and before the leading edge of the ejecta. In addition, the study showed that sheaths associated with strong and fast ejecta crossed at intermediate distances from the center have the strongest ULF power and largest variation in power throughout the sheath region. However, it is not well known how solar wind parameters vary within the sheath in general.

In this paper we present the first comprehensive investigation of how solar wind parameters that are of key importance to space weather vary in CME-driven sheath regions. Our aim is to answer the following science questions: (1) How do the properties and geoeffectiveness of sheaths depend on the properties of the driving ejecta? and (2) Is there a part of the sheath which is expected to be typically most geoeffective? The paper is organized as follows: In section 2 we present our data and methods, in section 3 we present the results of our statistical study, and in section 4 we discuss our results and conclusions.

2. Data and Methods

For this study, 1-min OMNI data have been used. The OMNI data set has been chosen because it provides near-continuous coverage of two solar cycles (Solar Cycle 23 and Solar Cycle 24), and 1-min resolution is sufficient to accurately track the variation of various plasma and geoeffective parameters within CME sheaths that have a typical duration of ∼ 9–12 hr at 1 AU (e.g., Kilpua, Koskinen et al., 2017). The parameters investigated are the IMF magnitude, IMF north-south magnetic field component in Geocentric Solar Magnetospheric (GSM) coordinates (B_Z), IMF root-mean-square fluctuations, solar wind speed, density, dynamic pressure, driving electric field ($E_Y \approx -V_X B_Z$, where V_X is the GSM X component of the solar wind velocity), and Alfvén Mach number. OMNI parameters have also been used to calculate the position of the subsolar magnetopause according to the Shue et al. (1998) model, which depends on dynamic pressure, and the IMF B_Z, that is, including both the effect of compression and the earthward erosion of the magnetopause during southward IMF. In this study, we have considered the absolute values of B_Z and E_Y ($|B_Z|$ and $|E_Y|$) since our aim has been to investigate the general potential of sheaths to generate out-of-ecliptic fields. We note that fluctuations in the IMF at various frequencies affect magnetospheric dynamics (see e.g., discussion in Kilpua, Balogh et al., 2017, and references therein). We chose to use here the 1-min fluctuations as they are directly given in the OMNI data set we use. The 1-min fluctuations correspond to the upper end of the Pc4 range (∼ 45 to ∼ 150 s) geomagnetic fluctuations and are close to the lower limit of the ULF Pc5 range (∼ 3–10 min) fluctuations. Pc5 and the highest period Pc4 fluctuation powers in the solar wind and magnetosphere are known to correlate (e.g., Kessel et al., 2004), and these fluctuations have profound effects in the magnetosphere, for example, for radiation belt electron dynamics (e.g., Elkington et al., 2003). Solar wind fluctuations are also known to enhance viscous interactions at the magnetopause and consequently the solar wind-magnetosphere coupling efficiency (e.g., Borovsky & Funsten, 2003; Osmane et al., 2015) and affect the conditions and thickness of the magnetospheric boundary layers (e.g., Nykyri & Dimmock, 2016).

To estimate the level of geomagnetic activity, 1-min *AL* and *SYM-H* indices and northern polar cap potential (PCN) have been used (for a discussion on these different geomagnetic indices, see, e.g., Mayaud, 1980). The *AL* index is obtained from magnetometer stations, typically 10–12, at high latitudes. It gives a proxy for the intensity of the westward electrojet and can thus be used as an indicator of substorm activity. The PCN is calculated using only one station at the northern polar cap that measures ionospheric currents which vary according to the magnetospheric convection. The *SYM-H* index measures disturbances in the longitudinally symmetric horizontal component of the geomagnetic field and is calculated from six low-latitude to midlatitude stations that are evenly distributed in longitude. While the lag between solar wind conditions and the response in auroral indices (*AL* and PCN) is only a few tens of minutes, it is clearly longer (∼ 1–1.5 hr) for ring current indices (*Dst* and *SYM-H*) as the ring current develops more slowly (e.g., Myllys et al., 2016, and references therein).

The sheaths that we studied were identified with the aid of the NASA-*Wind* interplanetary CME list (found at https://wind.nasa.gov/ICMEindex.php; see also Nieves-Chinchilla et al., 2018). The shock times were taken from the Heliospheric Shock Database (http://ipshocks.fi; see also; Kilpua, Lumme, et al., 2015). We made independent determinations of the ejecta leading edge times, although in most cases the times matched well with those reported in the NASA-Wind list. Primary signatures for determining the ejecta leading edge were sharp decreases in solar wind temperature and plasma beta and the start of smooth rotation of the magnetic field direction (e.g., Kilpua, Koskinen et al., 2017; Richardson & Cane, 1995; Zurbuchen & Richardson, 2006). In many cases, the sheath-ejecta boundary (and the ejecta trailing boundary) were

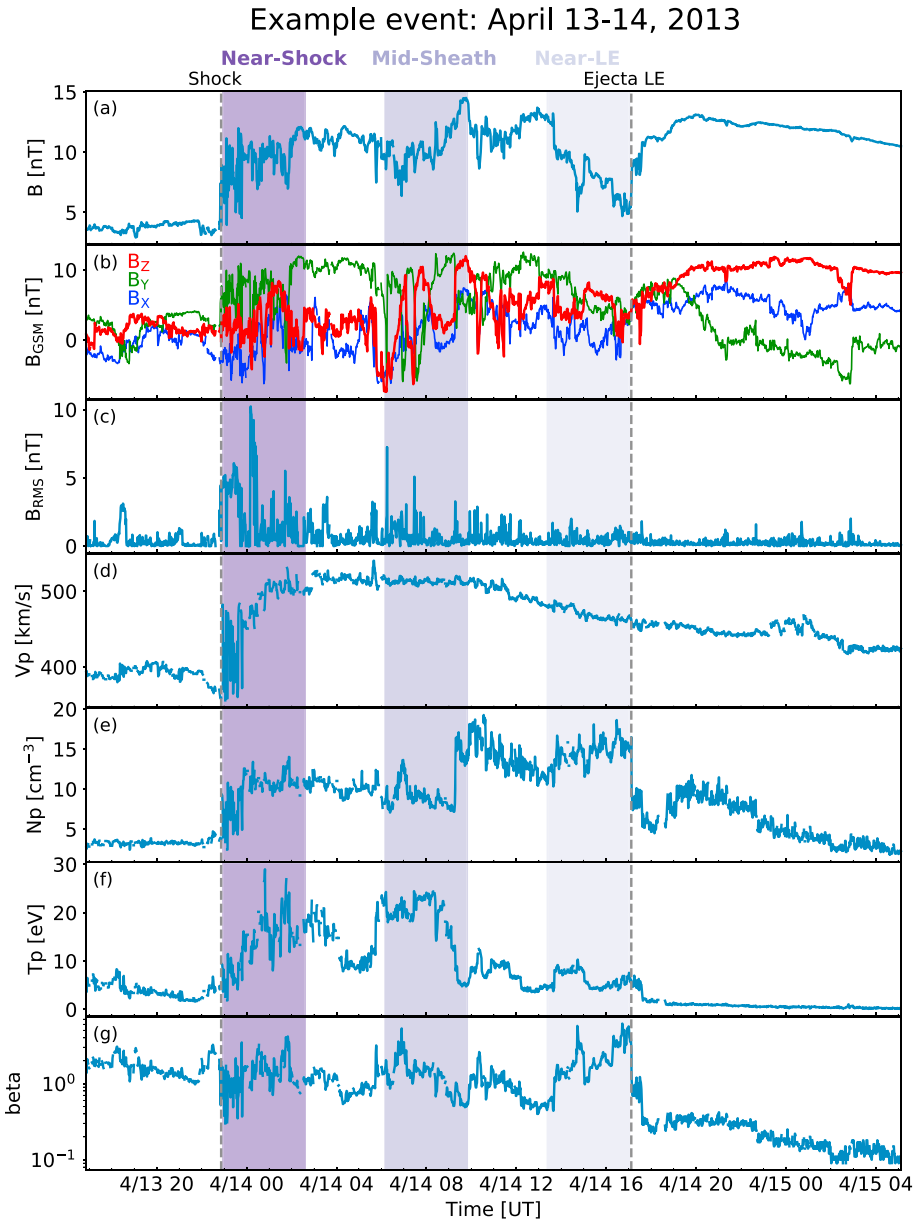

Figure 1. An example event showing IMF and solar wind plasma parameters during a sheath region observed in the near-Earth solar wind on 13–14 April 2013. The panels show the IMF (a) magnitude, (b) components in GSM (B_Z in bold), and (c) root-mean-square of the field vector and the solar wind (d) speed, (e) proton density, (f) temperature, and (g) plasma beta. The vertical dashed lines indicate the shock and ejecta LE observation times. Shaded regions indicate the near-shock (dark purple), midsheath (medium purple), and near-LE subregions (light purple), each spanning 20% of the total sheath duration. IMF = interplanetary magnetic field; GSM = Geocentric Solar Magnetospheric; LE = leading edge.

marked by magnetic holes (Wei, Liu, Fan, et al., 2003; Wei, Liu, Feng, et al., 2003). Only cases where the boundary was relatively clear have been included. Sheaths behind shocks that have propagated into a preceding ICME have also been excluded from this study. Our final sheath event list contains observations of 89 sheath regions (see the list from the supporting information). The duration of the sheaths under study ranges from 3.0 to 22.6 hr, with a mean duration of 10.2 hr.

Figure 1 shows an example sheath that was observed on 13–14 April 2013. The enhanced variability of the magnetic field (Figure 1c) with respect to the preceding ambient wind and the ejecta is clearly visible, as is the relatively high density (Figure 1e) and temperature (Figure 1f). The characteristically high variability in various other plasma parameters from the shock to the ejecta leading edge can also be noted.

Table 1
Criteria Used to Sort Sheaths Into Different Subgroups (A and B)

	Subset A			Subset B		
	Criteria	*N*	Samples	Criteria	*N*	Samples
V_{LE}	> 550 km/s	35	14,630	< 450 km/s	32	23,559
V_{exp}	> 50 km/s	20	9,352	< 5 km/s	17	9,771
$\Delta V_{LE,sw}$	> 150 km/s	29	11,924	< 80 km/s	30	21,160
B_{LE}	> 18 nT	27	12,788	< 14 nT	33	21,473
d_{SH}	< 0.08 AU	25	6,670	> 0.15 AU	22	20,753
C_{mag}	FR, $y_0/R < 0.25$	27	10,816	complex	20	14,540
θ_{FR}	< 45°	48	27,128	> 45°	28	17,302

*Note.*Columns *N* and "Samples" give the number of sheaths and the total number of 1-min data points in each subgroup. The parameters considered are, from top to bottom, ejecta leading edge speed (V_{LE}), ejecta expansion speed (V_{exp}), speed difference between ejecta and background wind ($\Delta V_{LE,sw}$), magnetic field strength at the ejecta leading edge (B_{LE}), sheath thickness (d_{SH}), magnetic coherence (C_{mag}, and where y_0/R is the ratio of the closest approach distance of the spacecraft from the FR center to the FR radius; see Thernisien et al., 2009), and FR inclination (θ_{FR}).

The purple-shaded regions in Figure 1 delimit three representative sheath subregions used in this analysis: the *near-shock* region (dark purple) covering 20% of the sheath closest to the shock; the *midsheath* region (medium purple) covering 20% of the sheath centered at the midpoint of the sheath; and the *near-LE* region (light purple) covering 20% of the sheath closest to the ejecta leading edge (LE). The 5 min closest to the shock and the ejecta leading edge have been excluded from the near-shock and near-LE regions, respectively.

Variations of the plasma parameters, IMF parameters, and geomagnetic response have been investigated with a superposed epoch analysis. In order to perform this analysis, all sheaths were resampled to the same average duration. Similarly to Kilpua et al. (2013), the 1-hr intervals after the shock and adjacent to the ejecta leading edge were not resampled because important microscale physical processes are expected to take place in these regions. We also included the 5 hr of solar wind preceding the shock and the 5 hr of ejecta after the end of the sheath. For each 1-min step of each parameter, the median, the lower quartile, and the upper quartile were calculated.

The list of sheaths has been sorted into two varying subsets according to the following ejecta properties: ejecta leading edge speed (V_{LE}) and magnetic field magnitude (B_{LE}), expansion speed of the ejecta (V_{exp}), speed difference between V_{LE} and the preceding solar wind ($\Delta V_{LE,sw}$), magnetic coherence of the ejecta (C_{mag}, that is, FR or non-FR/complex ejecta), and inclination of the FR axis (θ_{FR}) with respect to the ecliptic plane. The sheaths were also divided according to their thickness (d_{SH}), which could give a rough indication of the impact parameter (since sheath thickness increases from the nose of the CME toward its flanks). Table 1 lists the sorting criteria and the number of events in each subset. V_{LE} and B_{LE} were calculated by averaging the 1-min OMNI speed and IMF magnitude data over the first 2 hr of the ejecta. V_{exp} is defined here as half the difference between the leading and trailing edge speeds of the ejecta (e.g., Owens et al., 2005), where the trailing edge speed is calculated by averaging the 1-min OMNI data over the last 2 hr of the ejecta. Division of the ejecta into FR ejecta and non-FR ejecta is based on the identifications in the NASA-Wind ICME list and in the Richardson and Cane ICME list (http://www.srl.caltech.edu/ACE/ASC/DATA/level3/icmetable2.htm) described in Richardson and Cane (2010). In the NASA-Wind ICME list, events are divided into FRs, when a monotonic magnetic field rotation is observed, and ejecta, when no ordered topology is present. In the Richardson and Cane ICME list, a three-scale classification is used to divide the events into obvious magnetic clouds (2), events where some field rotation is present but that lack other key magnetic cloud signatures (1), and events that completely lack a magnetic cloud structure (0). We required for the FR-type ejecta that the event was classified as FR both in the NASA-Wind list and as magnetic cloud (2) in the Richardson and Cane list. Additionally, we also required for an FR-type ejecta classification a close encounter with respect to the FR central axis, defined by the impact parameter (y_0/R, where y_0 is the closest

approach distance from the FR center and R is the FR radius) in the NASA-Wind list to be < 0.25. The impact parameters in the list are obtained from fitting the circular-cylindrical FR analytical model (Nieves-Chinchilla et al., 2016). The FR division between low- and high-inclination FRs was also determined from the fitting results given in the NASA-Wind catalogue, that is; FR inclination angles $\theta_{FR} > 45°$ were defined as high inclination and $\theta_{FR} < 45°$ were defined as low inclination. Such division corresponds well to a determination based on visual inspection of the IMF B_Z rotation. The B_Z rotation is bipolar (i.e., its sign changes) in low-inclination FRs and unipolar (i.e., it maintains its sign) in high-inclination FRs (e.g., Bothmer & Schwenn, 1998; Huttunen et al., 2005; Mulligan et al., 1998). For the events that were not included in the NASA-Wind catalogue (six in total), visual inspection was used to determine the FR inclination.

3. Statistical Results

3.1. Overall Sheath Properties

First we consider the overall solar wind conditions within the sheaths under study and the geomagnetic activity at Earth during the passage of these sheaths. Second, we analyze how the sheaths' properties and geomagnetic response depend on the driving ejecta properties

3.1.1. Comparison With Ambient Conditions

Figure 2 shows the superposed epoch profiles of the selected solar wind parameters, subsolar magnetopause position from the Shue et al. (1998) model, and geomagnetic indices for the 89 sheaths and surrounding plasma (5-hr intervals ahead and behind). The interval ahead of the sheath represents the quiet ambient solar wind, and the interval after represents the CME ejecta. The IMF magnitude (B, Figure 2a) and out-of-ecliptic component ($|B_Z|$, Figure 2b), as well as the solar wind speed (V_p, Figure 2d), driving electric field ($|E_Y|$, Figure 2e), density (N_p, Figure 2f), and dynamic pressure (P_{dyn}, Figure 2g) increase abruptly at the transition into the sheath and remain high throughout the sheath interval. This is the expected behavior for compressed solar wind structures such as CME-driven sheaths. The lower N_p and P_{dyn} in the ejecta compared to the sheath reflect the significant expansion typically undergone by ejecta after their launch from the Sun (e.g., Klein & Burlaga, 1982; Kilpua, Koskinen et al., 2017). However, despite significant expansion in the corona and interplanetary space, the ejecta typically have strong magnetic fields and consequently high $|E_Y|$ values. This is due to their initially very high magnetic fields when launched from the Sun (e.g., Carley et al., 2017; Tun & Vourlidas, 2013). The level of IMF fluctuations (B_{RMS}, Figure 2c) also increases sharply from the preceding solar wind into the sheath and is substantially higher in the sheath than in the ejecta. The Alfvén Mach number (M_A, Figure 2h) is approximately at the same level in the sheaths as in the preceding solar wind, and declines strongly in the ejecta. The subsolar magnetopause (R_{mp}, Figure 2i) is most compressed during the sheath passage due to the high P_{dyn} in the sheath. The *SYM-H* index (Figure 2j) starts to decrease (i.e., indicating enhanced geomagnetic activity) during the sheath and continues to decline during the ejecta, while PCN and *AL* indices (Figure 2k and Figure 2l) do not show substantial differences between sheath and ejecta.

3.1.2. Dependence on Ejecta Properties

We now consider how overall sheath properties depend on the properties of the driving ejecta. Table 2 lists the median values within the sheaths of the same set of parameters as in Figure 2. The sheaths have been separated into different subsets using the criteria we defined in section 2; see Table 1.

It can be seen in Table 2 that the values associated to ejecta leading-edge speed (V_{LE}), leading-edge magnetic field magnitude (B_{LE}), expansion speed (V_{exp}), and speed difference between V_{LE} and the ambient solar wind ($\Delta V_{LE,sw}$) reveal clear differences in the median values of the sheath parameters between the subsets A and B. In turn, the remaining sorting criteria shown in Table 2, that is, sheath thickness (d_{SH}), magnetic coherence (FRs and non-FRs, C_{mag}), and FR inclination (θ_{FR}), reveal relatively weak dependencies. We note that the sheaths of complex ejecta (non-FR ejecta) have a tendency to be slightly faster and more geoeffective in terms of the *AL* index than the sheaths of the FR type ejecta that are crossed centrally (i.e., the impact parameter $y_0/R < 0.25$, see section 2). Complex ejecta also clearly have larger median magnetic field fluctuations than FRs. In addition, Table 2 shows that the medians of the distributions A and B are very similar according to V_{LE}, V_{exp}, and $\Delta V_{LE,sw}$. These similarities are expected as V_{LE} is known to correlate strongly with both V_{exp} and $\Delta V_{LE,sw}$ (e.g., see Owens et al., 2005). We therefore further investigate only the distributions sorted according to V_{LE} and B_{LE} below.

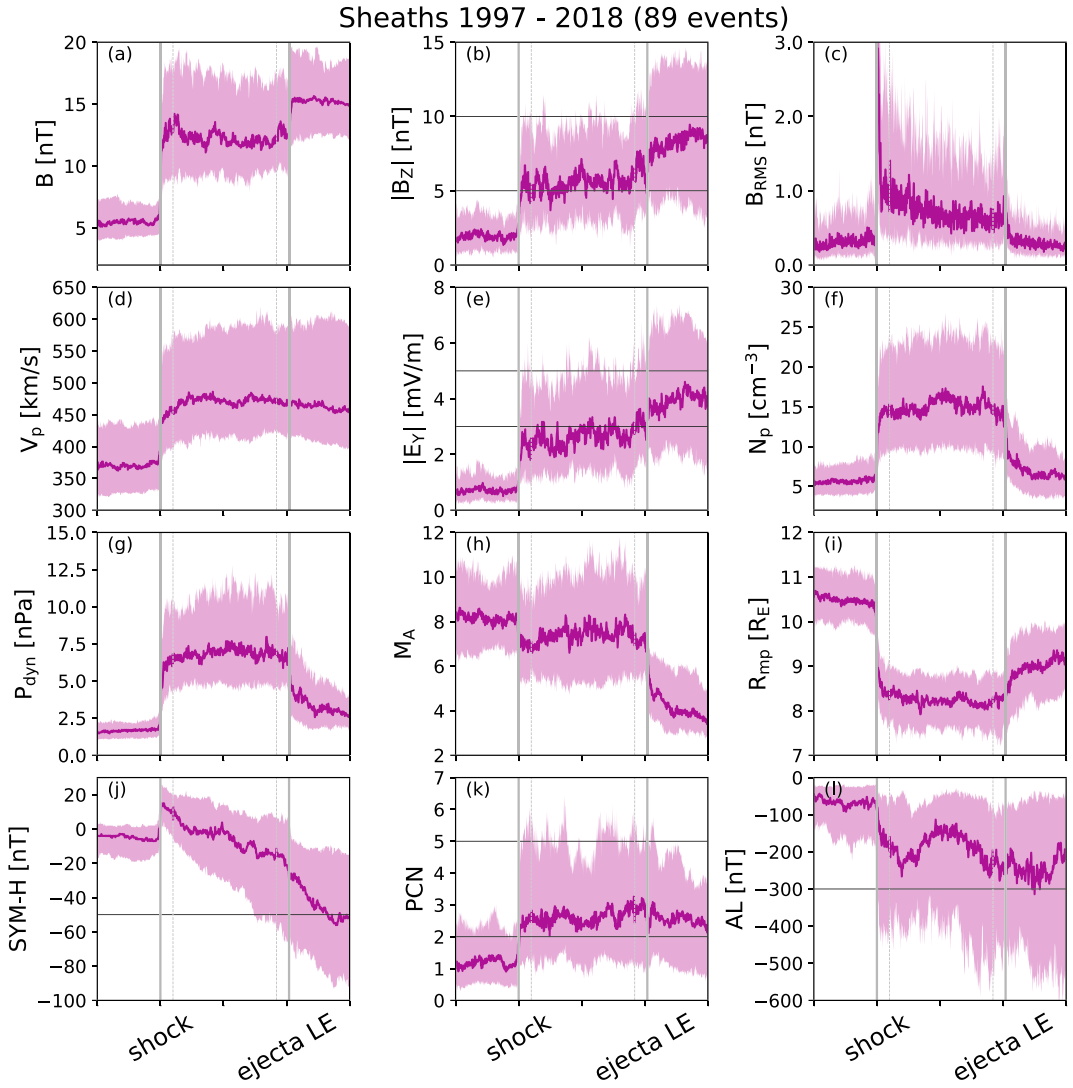

Figure 2. Averaged variations in solar wind parameters and geomagnetic response for the 89 sheaths analyzed. Curves show the median values, and shaded regions indicate the lower to upper quartile range. The panels show distributions of the (a) *B* field magnitude, (b) absolute value of the north-south *B* field component in GSM coordinates, and (c) root-mean-square of the *B* field vector. Also shown are the solar wind (d) speed, (e) proton density, (f) dynamic pressure, (g) absolute value of the electric field *Y* component, and the (h) Alfven Mach number, (i) subsolar magnetopause position from the Shue et al. (1998) model, and the (j) *SYM-H*, (k) PCN, and (l) *AL* indices. In panels (b), (e), and (j)–(l) the horizontal lines indicate the thresholds for moderate and strong solar wind forcing and geomagnetic activity; see text for details. Gray solid lines bound the sheath region (resampled to same duration). Gray dashed lines show the limits of the 1-hr regions in the sheaths that were not resampled. Five-hour intervals before the shock and within the ejecta are also included in the plots. GSM = Geocentric Solar Magnetospheric; PCN = polar cap potential; LE = leading edge.

The histograms in Figure 3 show the distributions of the 1-min OMNI data using 50 bins for all sheaths preceding the slow (blue: $V_{LE} < 450$ km/s) and fast (red: $V_{LE} > 550$ km/s, circle markers) ejecta, respectively. Violet regions are those where the fast- and slow- ejecta distributions overlap. To get information on how individual sheaths affect the distributions, the curves in the figures show the corresponding relative sheath frequency distributions as a function of their median (strong solid curves) and the 90th percentile (lighter dashed curves) using ten bins. The 90th percentile indicates the values below which 90% of observations fall, giving thus insight on the contributions of individual sheaths to the peak values in distributions for the whole subset. Figure 4 shows the corresponding information for the sheaths preceding the weak (green: $B_{LE} <$ 14 nT) and strong (orange: $B_{LE} > 18$ nT) ejecta. The brown-yellow regions are now those where the strong- and weak- ejecta sheath distributions overlap. Moreover, Figure 5 shows the relative sheath frequency

Table 2
Median Values of Distributions of the Selected Solar Wind Parameters and Geomagnetic Indices for the Sheaths in Different Subsets (see Table 1)

	B (nT)	B_Z (nT)	B_{RMS} (nT)	V_p (km/s)	N_p (cm^{-3})	P_{dyn} (nPa)	E_y (mV/m)	M_A	R_{mp} (R_E)	*SYM-H* (nT)	PCN	*AL* (nT)
V_{LE}	16.5/10.7	7.7/5.1	0.97/0.51	616/398	10.8/19.8	8.4/6.1	4.7/2.0	6.3/8.1	7.9/8.5	−21/2	3.9/2.0	−349/−123
V_{exp}	14.1/11.4	7.1/5.7	0.84/0.51	617/417	9.3/17.4	6.5/6.0	4.2/2.4	6.1/7.4	8.0/8.4	−22/−4	3.9/2.1	−379/−168
$\Delta V_{LE,sw}$	17.5/9.6	7.7/4.3	1.08/0.48	620/422	12.7/16.2	9.5/5.6	4.7/1.9	6.3/8.8	7.7/8.6	−14/3	3.5/1.9	−366/−132
B_{LE}	18.4/9.5	7.3/4.4	0.87/0.48	484/457	22.6/11.8	10.1/4.9	3.6/2.0	5.9/8.0	7.7/8.8	−1/−4	3.0/1.9	−234/−141
d_{SH}	12.0/10.2	5.4/4.8	0.60/0.60	497/400	19.1/13.5	7.0/6.5	2.7/2.0	8.7/7.6	8.3/8.4	1/−4	2.5/2.4	−149/−203
C_{mag}	10.8/12.0	5.8/5.3	0.52/0.81	450/535	14.1/13.0	5.6/6.7	2.5/2.8	7.7/7.1	8.6/8.3	−4/−8	2.0/3.3	−173/−239
θ_{FR}	10.9/12.3	5.0/5.4	0.57/0.60	438/457	16.3/15.4	6.1/6.6	2.2/2.5	8.0/7.1	8.5/8.3	2/−6	2.1/2.6	−141/−199

Note. The sorting is made according to the ejecta leading edge speed (V_{LE}), ejecta expansion speed (V_{exp}), speed difference between V_{LE} and preceding solar wind ($\Delta V_{LE,sw}$), ejecta leading edge magnetic field magnitude (B_{LE}), sheath thickness (d_{SH}), magnetic coherence of the ejecta (FR ejecta with $y_0/R < 0.25$ or non-FR ejecta; C_{mag}), and FR axis inclination with respect to the ecliptic (θ_{FR}). The columns give medians of the IMF magnitude (B), IMF north-south component in GSM (B_Z), root-mean-square of the field vector (B_{RMS}), solar wind speed (V_p), proton density (N_p), dynamic pressure (P_{dyn}), electric field (E_y), Alfvén Mach number (M_A), subsolar magnetopause position from the Shue et al. (1998) model (R_{mp}), and the *SYM-H*, PCN, and *AL* indices. The medians are provided in the format Subset A/Subset B. LE = leading edge; FR = flus rope; IMF = interplanetary magnetic field.

distributions as a function of the percentage of the sheath in 10% bins covered by moderate and intense solar wind forcing and geomagnetic response (e.g., Gonzalez et al., 1994; Stauning, 2013; Vorobjev et al., 2018) and the periods when the subsolar magentopause was pushed below $< 8\ R_E$ and below geostationary orbit (i.e., $<\ 6.6\ R_E$). The values in parenthesis give the percentage for the whole sheath population when these thresholds were exceeded. We performed also a nonparametric Mann-Whitney-Wilcoxon U test (Storch & Zwiers, 1999) for each case to investigate whether differences in distributions are statistically significant. The event and sample sizes for the red and blue subsets are given in Table 1. For all cases, very small p values were obtained (practically $p \approx 0$), signifying that distributions were taken from different populations.

The top panels of Figures 3 and 4 show that the sheaths preceding fast and strong ejecta tend to have stronger B, $|B_Z|$, and B_{RMS} than the sheaths associated with slow and weak ejecta. When sheaths are sorted according to V_{LE}, the median B, $|B_Z|$, and B_{RMS} for the whole subset are 57%, 50%, and 90% larger, respectively, for the fast-ejecta sheaths than for the slow-ejecta sheaths, and the fast-ejecta sheath distribution is heavier tailed at large values. The division according to B_{LE} separates the sheaths even more distinctly those with weaker and stronger magnetic fields; now the median B and $|B_Z|$, are 94% and 66% larger for the strong-ejecta sheaths than for the weak-ejecta sheaths and their B field histograms (Figure 4) in particular show only a little overlap. The strong-ejecta sheaths have also stronger fluctuations; for example, their median B_{RMS} for the whole subset is 82% larger than for the weak-ejecta sheaths. The sheath frequency distributions in Figures 3 and 4 show that the fast- and strong-ejecta sheaths have a larger spread in their B and $|B_Z|$ medians than the slow- and weak-ejecta sheaths, but their 90th percentile curves suggest that a large part of the events contribute to the heavy tails in histograms. Only the most extreme values ($B \gtrsim 30$ nT and $|B_Z| \gtrsim$ 20–25 nT) seem to belong to only a few events. The B_{RMS} values are generally small ($\lesssim 2$), and the medians have a narrow spread for all investigated divisions here. The 90th percentile B_{RMS} values however show that the majority of sheaths embed also large fluctuations. The top panels in Figure 5 further show that nearly all fast-ejecta and strong-ejecta sheaths in our study are at least 40% covered by moderately out-of-ecliptic fields ($|B_Z| > 5$ nT) and the coverage peaks in the 60–80% bins. Most slow-ejecta sheaths also have a significant coverage of $|B_Z| > 5$ nT, while the majority of weak-ejecta sheaths are biased toward low coverage. Strongly out-of-ecliptic fields ($|B_Z| > 10$ nT) are in turn embedded mostly in the fast-ejecta and strong-ejecta sheaths, although only in a few events the coverage exceeds 50%. It is however notable that there are a few slow- and weak-ejecta sheaths with a considerable coverage of $|B_Z| > 10$ nT. These findings are also in agreement with the percentages of data points in all sheaths in a given subset exceeding these thresholds (see the values in parenthesis in Figures 5a and 5b): 65% of the fast-ejecta sheath $|B_Z|$ samples are > 5 nT, and 36% > 10 nT, while the corresponding percentages for the slow-ejecta sheath samples are 50% and 16%. The strong-ejecta sheaths have very similar percentages as the fast sheaths, while the weak-ejecta sheaths have corresponding percentages only of 44% and 11%.

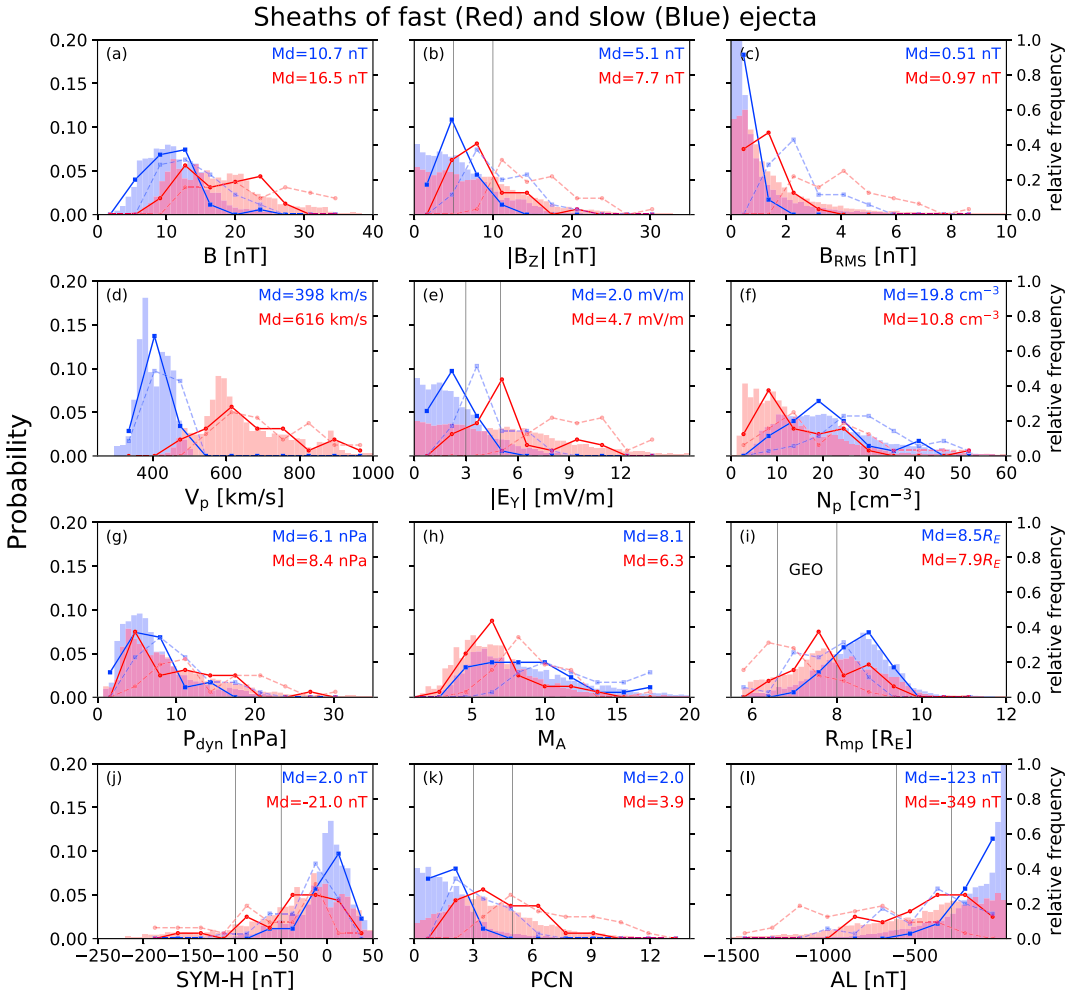

Figure 3. Probability distributions of various solar wind and geomagnetic parameters for the sheaths of fast (red and circle markers; leading edge speed $V_{LE} > 550$ km/s) and slow (blue and square markers; $V_{LE} < 450$ km/s) ejecta. Violet regions indicate where the blue and red subsets overlap. The panels show the same parameters as in Figure 2. The curves give the relative sheath frequency distributions as a function of median (solid) and 90th percentile (dashed) of different parameters. The vertical lines in panels (b), (e), and (j)–(l) show the threshold values for moderate and intense out-of-ecliptic fields, solar wind driving E field, and geomagnetic response; see text for details. In Panel (i), the first vertical line indicates the geostationary orbit (6.6 R_E) and the second 8 R_E (our criteria for the significant compression). LE = leading edge.

The ejecta leading edge speed separates sheaths distinctly into slow and fast populations as shown in Figure 3d): The sheaths of fast ejecta (red subset) are much faster than the sheaths of slow ejecta (blue subset). The median speed for the whole red subset is 616 km/s, while that of the blue subset is only 398 km/s, with very little overlap between the histograms. Due to their tendency to have stronger IMF $|B_Z|$ and higher solar wind speeds, the fast-ejecta sheaths have also considerably larger solar wind driving electric fields, $|E_Y|$ (Figure 3e), the median $|E_Y|$ being 135% larger for the fast-ejecta sheath than for the slow-ejecta sheath subset, and the red distribution is considerably flatter and heavier-tailed at large $|E_Y|$ compared to the blue distribution, which is clustered at small $|E_Y|$ values. The median and 90th percentile V_p and $|E_Y|$ curves are also clearly separate for the fast- and slow-ejecta sheaths. While the most extreme speeds ($\gtrsim$ 800 km/s) and driving electric fields ($|E_Y| \gtrsim 12$ mV/m) are associated to a few events only, the majority of the fast-ejecta sheaths contribute to the heavy tail in the distribution. In turn, the division according to B_{LE} does not separate sheaths into slow and fast populations (Figure 4d); the orange and green histograms are now very similar and have similar medians. The sheaths of the strong ejecta have in turn a tendency toward higher $|E_Y|$ (Figure 4e), with a larger (80%) median and heavier-tailed distribution. Due to their similar speeds, the differences between the strong- and weak-ejecta subsets are not as clear as when sorting with V_{LE}. The

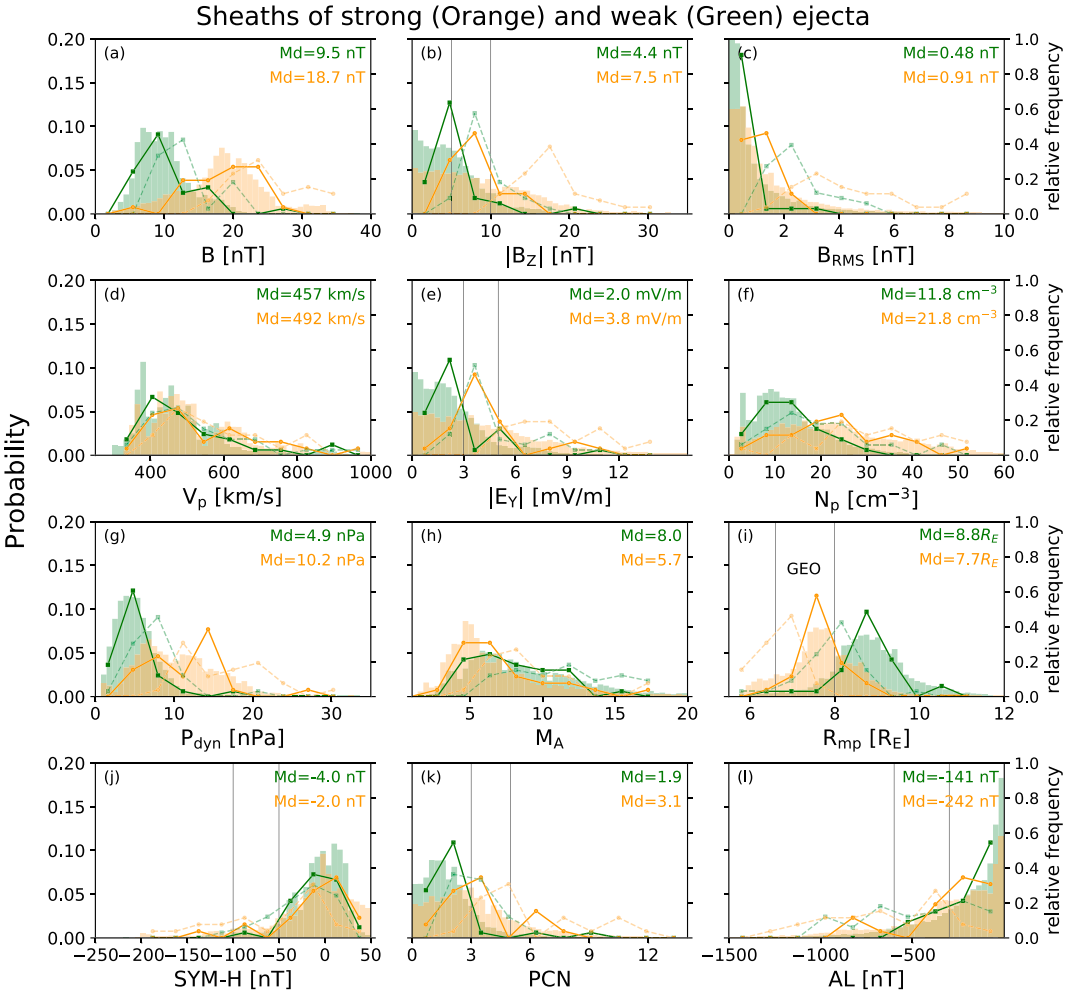

Figure 4. Probability distributions of various solar wind and geomagnetic parameters for the sheaths related to strong (orange and square markers; leading edge field magnitude $B_{LE} > 18$ nT) and weak (green and circle markers; $B_{LE} < 14$ nT) ejecta. The different panels are presented in the same format as Figure 3. The curves give the relative sheath frequency distributions as a function of median (solid) and 90th percentile (dashed) of different parameters. LE = leading edge.

90th quartiles show again that the majority of the strong-ejecta sheaths contributed to the heavy $|E_Y|$ tail. Figures 5c and 5d show that similarly to moderately out-of-ecliptic fields, both the fast- and strong-ejecta sheaths have a high coverage of moderate driving electric field values ($|E_Y| > 3$ mV/m), while the slow- and weak-ejecta sheaths are biased toward < 40 % coverage. The fast-ejecta sheaths have the largest coverage of intense $|E_Y|$ values ($|E_Y| > 5$ mV/m), peaking in the 30–60% bins, while the clear majority of slow- and weak-ejecta sheaths have < 10% contribution from intense $|E_Y|$. Figure 5 also shows that in total 66% of the fast-ejecta data points indicate moderate driving and 48% intense driving, while the corresponding percentages are significantly lower for the slow-ejecta subset, at 30% and 10%, respectively. The strong-ejecta sheaths have smaller percentage of intense $|E_Y|$ values (36%) than the fast-ejecta sheaths. The weak-ejecta sheaths in turn have considerably larger percentages of both moderate and intense $|E_Y|$ values than the slow-ejecta sheaths (50% and 16%). This is due to their tendency toward higher speeds.

Distributions of the solar wind density N_p (Figures 3f and 4f) reveal some notable features. The slow-ejecta sheaths are on average considerably denser than the fast-ejecta sheaths: The median density for the blue subset is 19.8 cm^{-3}, while for the red subset it is only 10.8 cm^{-3}; that is, the median density is 83% larger for the slow-ejecta sheaths. Both distributions are heavy tailed, but the blue distribution is clearly broader and peaks at larger N_p values. The sheaths of strong ejecta, however, have clearly larger densities than the weak-ejecta sheaths; the median N_p is 22.6 and 11.8 cm^{-3} for the orange and green distributions, respectively,

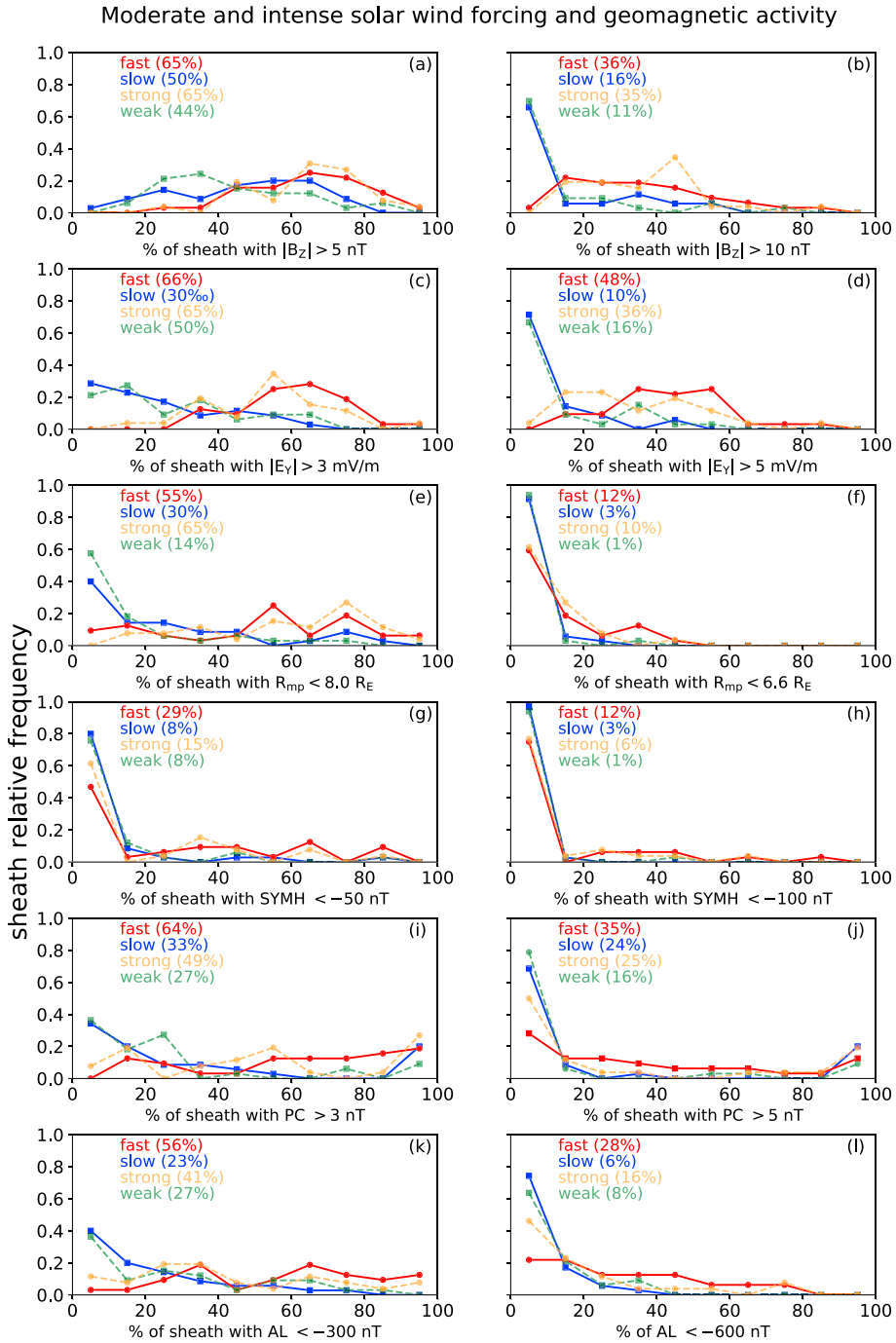

Figure 5. The relative sheath frequency distribution as a function of percentage covered of the sheath by the moderate and intense out-of-ecliptic fields B_Z (a and b), solar wind driving electric fields $|E_Y|$ (c and d), *SYM-H* (g and h), PCN (i and j), and *AL* (k and l). Panels (e) and (f) show the percentages of the sheath when the subsolar magnetopause was pushed below $< 8R_E$ and below geostationary orbit (i.e., $< 6.6R_E$), respectively. The red and blue curves with square markers show the results for the fast- ($V_{\mathrm{LE}} > 550$ km/s) and slow- ($V_{\mathrm{LE}} < 450$ km/s) ejecta sheaths, respectively. The orange and green curves with circle markers show the results for the strong- ($B_{\mathrm{LE}} > 18$ nT) and weak- ($B_{\mathrm{LE}} < 14$ nT) ejecta sheaths, respectively. The values in the parenthesis show the percentages of data samples that exceeded the thresholds for the whole sheath subsets. LE = leading edge.

that is, 92% higher for the strong-ejecta sheaths. The median and 90th percentile curves (Figures 3f and 4f) show that while the slow- and strong-ejecta sheaths have a large spread in their medians, the majority of them contribute to the high-density tail ($N_p > 20$ cm^{-3} values).

The $P_{\rm dyn}$ distributions are relatively similar between the fast- and slow-ejecta sheaths (Figure 3g). The reason for this stems from the fact that while the fast-ejecta sheaths are on average much faster than the slow-ejecta sheaths, they have typically considerable lower densities. The red $P_{\rm dyn}$ distribution is flatter and has a heavier tail, but as shown by the median and 90th percentile curves, the highest $P_{\rm dyn}$ values ($P_{\rm dyn} \gtrsim 20-25$ nPa) are related to only a few events. For the division according to $B_{\rm LE}$, in turn, the $P_{\rm dyn}$ values (Figure 4g) are much larger for the sheaths preceding the strong ejecta; here the median $P_{\rm dyn}$ is 10.2 nPa for the orange subset, 106% larger than the median $P_{\rm dyn}$ of 4.9 nPa for the green subset. There are only a very few $P_{\rm dyn} \gtrsim 20-25$ nPa values and sheaths having their 90th percentile curve beyond, but it is clear that the majority of the strong-ejecta sheaths contribute to the heavy tail at $P_{\rm dyn} \approx$ 10–20 nPa. The M_A distributions (Figures 3h and 4h.) for all investigated divisions are more similar; all lack very low M_A values ($M_A \lesssim 1$), and the distributions peak around $M_A \approx$ 5–7. The slow- and weak-ejecta sheath distributions have however the heaviest tails and the largest medians for the whole subset. Their median curves are also relatively broad and the 90th percentile curves fall quickly beyond $M_A \gtrsim$ 13–14.

Figures 3i, 4i, 5e, and 5f highlight that in particular the fast- and strong-ejecta sheaths effectively compress and erode the subsolar magnetopause from its nominal location, at about 10–12R_E. While the majority of the fast- and strong-ejecta sheaths compress the magnetopause beyond 8 R_E, and typically > 50% of the sheath duration, clearly less than half of them have > 10% coverage of the periods when the magnetopause is compressed beyond geostationary orbit. Periods of significant compression are considerably less common for the slow- and in particular for the weak-ejecta sheaths. Furthermore, Figure 5 shows that in total 12% of the fast-ejecta data points and 10% of the strong-sheath data points are < 6.6R_E, while for the slow and weak ejecta this occurs only for 3% and 1% of the time, consistent with our analysis above. The slow-ejecta sheath distribution has however a considerable amount of data points (30%) below 8 R_E, and the median and 90th percentile curves in Figure 3i show that a large fraction of sheaths contribute to these significantly compressed values.

Finally, Figures 3j–3l and 4j–4l show that the fast-ejecta sheaths are clearly more geoeffective than the slow-ejecta sheaths, while the geomagnetic responses are more similar between the sheaths related to the weak and strong ejecta. For the division according to $V_{\rm LE}$, the fast-ejecta sheath distributions for the *SYM-H*, PCN, and *AL* indices show heavier tails at disturbed values, while the corresponding slow-ejecta distributions are clustered at quiet values. The medians in particular for the fast-ejecta sheaths have a large spread, and it is clear that there are a very few data points with *SYM-H* < −100 nT. For the fast-ejecta sheath distribution in total 12% of the *SYM-H* data points are < −100 nT, while for the slow-, strong-, and weak-ejecta sheaths the percentages are only 3%, 6%, and 2%, respectively. The median, 90th quartile curves in Figures 3 and 4, and Figure 5h show that only a few events caused *SYM-H* to reach the intense storm limit. The moderate storm limit (*SYM-H* < −50 nT) was exceeded more frequently and for a larger fraction of time, in particular for the fast- and strong-ejecta sheaths, but again for all subsets there is a significant number of sheaths that caused only a weak or no geomagnetic response at all. For the fast-ejecta sheaths nearly one third of the data points (29%) exceeded the moderate storm limit. The strong-ejecta sheaths were again less efficient causing *SYM-H* disturbances; from them only 15% of the data points had *SYM-H* < −50 nT, and from the slow- and weak-ejecta sheath only 8%. A considerably larger fraction of sheaths however contribute to moderate and intense auroral and PCN activity. For example, 56% of the red data points indicate moderate auroral activity (*AL* < −300 nT) and 28% intense auroral activity (*AL* < −600 nT), while for the blue data points the corresponding percentages are only 23% and 6%, respectively. For the division according to $B_{\rm LE}$, 41% of the orange *AL* data points are < −300 nT and 16% < −600 nT, while for the green data points the corresponding percentages are 27% and 8.3%, respectively. In particular for the fast-ejecta sheaths, a large number of sheaths contribute to the high-*AL* and PCN tail. Figure 5 however shows that there is a large variability in the coverage of moderate and intense geomagnetic activity for all indices from event to event.

3.2. Variations Within the Sheath

For most of the investigated parameters, the superposed epoch analysis plots in Figure 2 do not reveal clear variations across the sheath. The most obvious trends are for $B_{\rm RMS}$ (Figure 2c) and for the *SYM-H* and *AL* indices (Figures 2j and 2l). $B_{\rm RMS}$ peaks in the near-shock region and decreases monotonically toward the

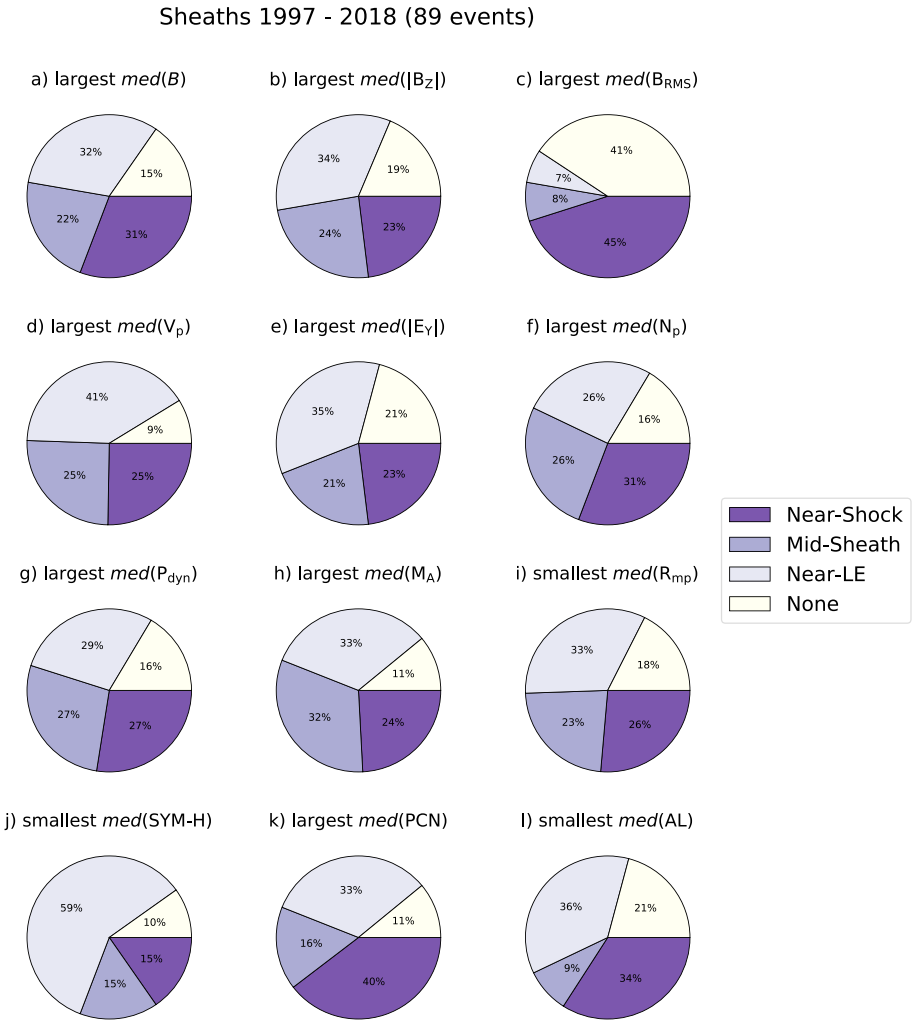

Figure 6. Donut diagrams showing the percentage of each subregion in which the median of the parameter exceeded the 60th percentile of two other subregions (or was less than the 40th percentile for R_{mp}, *SYM-H*, and *AL*). The parameters shown are the same as in Figure 2. PCN = polar cap potential.

ejecta LE. *SYM-H* decreases toward the ejecta LE as expected, because of the time it takes for the ring current to develop, while *AL* in turn peaks close to both the shock and ejecta LE. The lack of clear trends across the sheath could result from large variations in sheath properties from event to event (see, e.g., Figure 1).

To study the variations within individual sheaths, the median for each parameter were first calculated separately in the near-shock, midsheath, and near-LE regions. Then, it was determined for each of the subregions how many times the median exceeded the 60th percentile of the other two subregions (or was less than the 40th percentile for R_{mp}, *SYM-H*, and *AL*). The results are presented through donut diagrams in Figure 6. For example, Figure 6a shows that the largest median B ($med(B)$) occurred in 31% of the cases in the near-shock region, 32% of the cases in the near-LE region, and in 22% of the cases in the midsheath regions. In 15% of the cases, differences in the median B were not significant between the three subregions. The largest $med(|B_Z|)$ (Figure 6b) occurred most frequently in the near-LE region (34%, compared to 24% and 23% for the midsheath and near-shock regions, respectively), while the largest $med(B_{RMS})$ (Figure 6c) were typically found in the near-shock region (45% of the cases compared to only 8% and 7% for the midsheath and near-LE regions, respectively). We note, however, that in 41% of the cases the magnetic field fluctuations were distributed more evenly within the sheath. The largest median V_p and $|E_Y|$ (Figures 6d and 6e) were observed most often in the near-LE region, while the percentages for the median N_p, P_{dyn}, M_A, and R_{mp} (Figures 6g–6i) were distributed more evenly between the three subregions. The smallest $med(SYM-H)$ occurred in 59% of the cases in the near-LE region and, finally, Figures 6k and 6l show that the largest $med(PC)$ and smallest

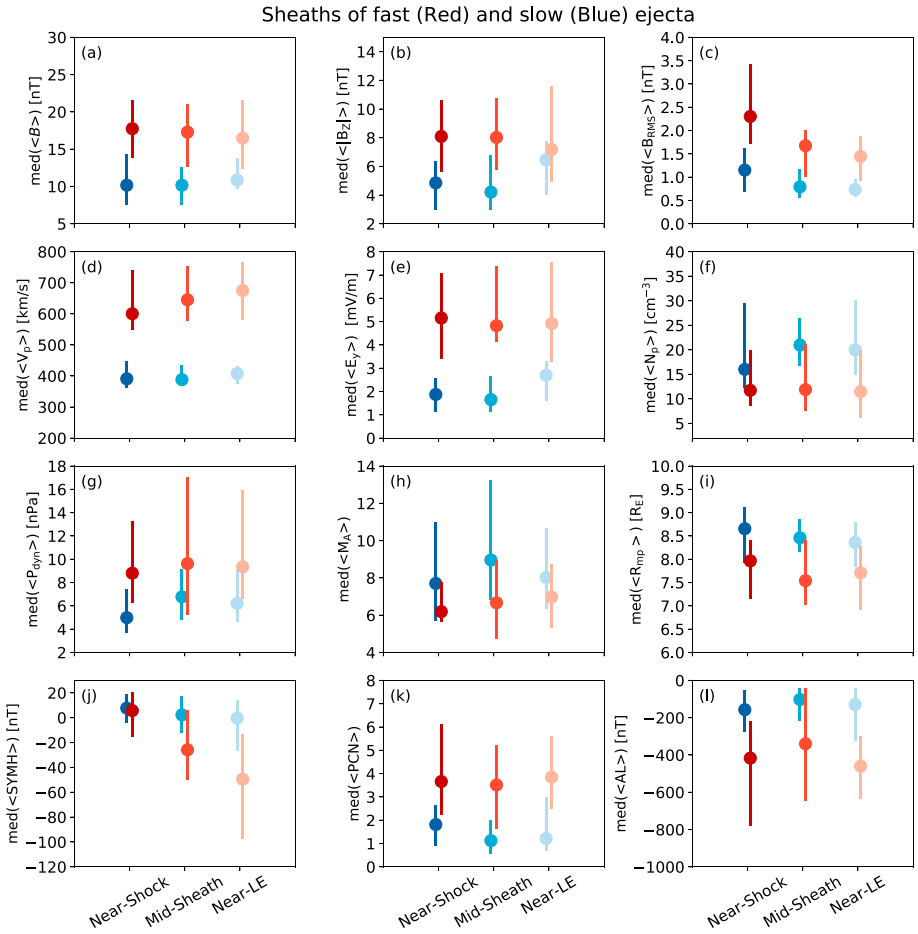

Figure 7. Medians of the average solar wind and geomagnetic parameters calculated separately for the near-shock, midsheath, and near-LE regions for the sheaths of fast (red; leading edge speed $V_{LE} > 550$ km/s) and slow (blue; $V_{LE} < 550$ km/s) ejecta. The vertical lines show the interquartile range. The panels show the same parameters as in Figure 2. LE = leading edge.

med(*AL*) occurred at similar frequencies in the near-shock and near-LE regions, while the midsheath region was clearly the least geoeffective, featuring largest *med*(PC) and smallest *med*(*AL*) only in 16% and 9% of the cases, respectively. We also note that pie diagrams for the main geoeffective parameters, that is, $|B_Z|$, V_p, and $|E_Y|$ agree well with *AL* and PCN, but for *SYM-H* the activity is biased in the near-LE region. This is likely attributed to ring current responding slower than auroral activity as discussed in section 2.

Figures 7 and 8 show the medians and interquartile ranges of the averages of the sheath parameters in the near-shock, midsheath, and near-LE regions for the sheaths preceding slow and fast ejecta and preceding weak and strong ejecta, respectively. In addition, for the same sorting criteria, Figures 9 and 10 show the fraction of sheath subregions that were covered by strongly out-of-ecliptic fields ($|B_Z| > 10$ nT) and high densities ($N_p > 20$ cm^{-3}).

For the fast-ejecta sheaths, the median $\langle B \rangle$ and $\langle |B_Z| \rangle$ decrease from the shock toward the ejecta LE, while for the sheaths of slow and strong ejecta the trend is opposite (Figures 7a, 7b, 8a, and 8b). For the sheaths of weak ejecta, in turn, the median $\langle B \rangle$ and $\langle |B_Z| \rangle$ show very little variations in different sheath subregions. For all cases shown, the median $\langle B_{RMS} \rangle$ (Figures 7c and 8c) are largest in the near-shock region and smallest in the near-LE region, consistent with our previous results. The top row of Figure 9 further shows that, for the sheaths of fast ejecta (red outer part of the donuts), there is no clear trend in how much out-of-ecliptic fields ($|B_Z| > 10$ nT) occupied different sheath subregions. The majority of the slow-ejecta sheaths, in turn, had a negligible incidence of $|B_Z| > 10$ nT; for the midsheath region, this is the case for as much as 74% of the studied events. The tendency of the near-LE region of the sheaths of strong ejecta to embed strongly out-of-ecliptic fields is also apparent in the top row of Figure 10. The near-LE region has a negligible amount

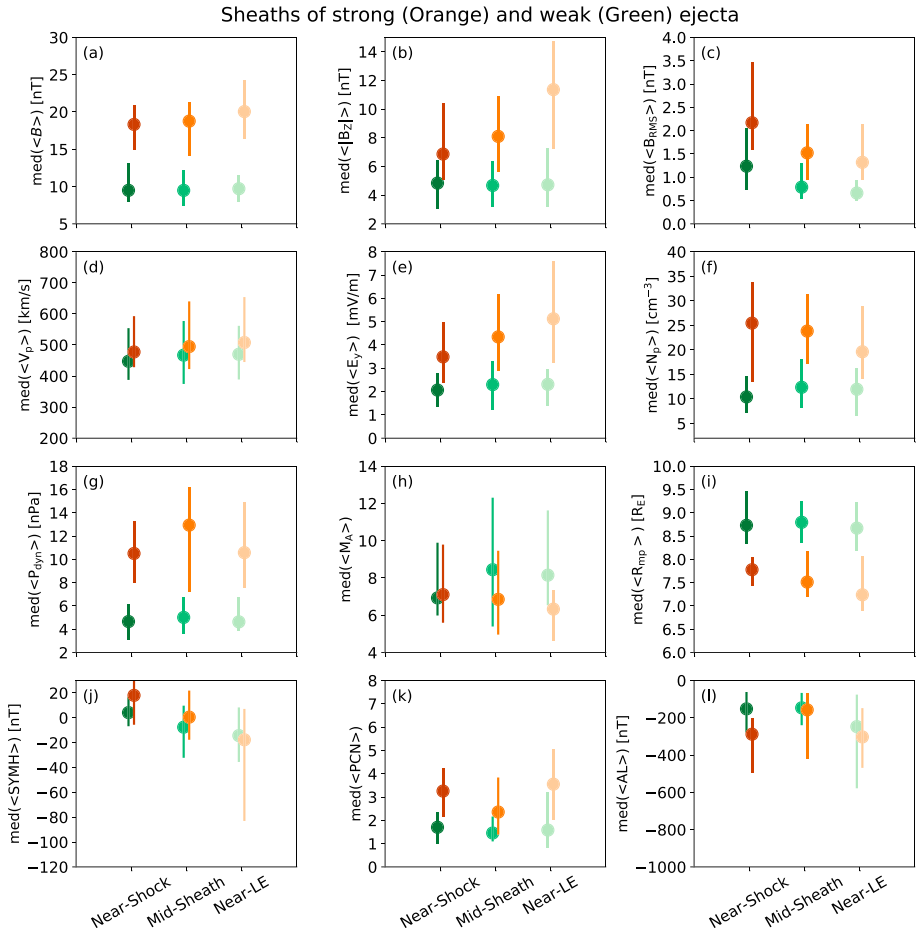

Figure 8. Median of the average solar wind and geomagnetic parameters calculated separately for the near-shock, midsheath, and near-LE regions for the sheaths of strong (orange; leading edge field $B_{\mathrm{LE}} > 18$ nT) and weak (green; $B_{\mathrm{LE}} < 18$ nT) ejecta. The vertical lines show the interquartile range. The panels are presented in the same format as in Figure 2. LE = leading edge.

of $|B_Z| > 10$ nT fields only in 11% of the cases, and in 37% of cases this subregion is dominated (i.e., incidence > 0.66) by strongly out-of-ecliptic fields. In comparison, in the near-shock and midsheath regions the latter occurred for only 7% and 11% of the cases. Weak-ejecta sheaths display in the majority of the cases a negligible amount of $|B_Z| > 10$ nT for all subregions. Table S2 in the supporting information shows that in all expect one case for the fast-ejecta and strong-ejecta sheaths the > 0.66 incidences do not overlap between different subregions. This gives also further support that histograms showing distributions of $|B_Z|$ in Figures 3 and 4 are not dominated by a few events only.

Figures 7d and 8d show that significant differences in the median $\langle V_p \rangle$ between different sheath subregions are found only for fast-ejecta sheaths. For them, the median speed increases from the shock to the ejecta LE. For the median $\langle |E_Y| \rangle$ in turn (Figures 7e and 8e), the most significant differences occur for strong-ejecta sheaths, for which the driving electric field values increase clearly from the shock to the ejecta LE.

The median $\langle N_p \rangle$, $\langle M_A \rangle$, and $\langle P_{\mathrm{dyn}} \rangle$ are generally stable across the sheath for both the fast and slow-ejecta sheaths, as shown in Figures 7f–7h . The clearest trend is that for the sheaths of slow ejecta (blue subset) the median $\langle N_p \rangle$ and $\langle P_{\mathrm{dyn}} \rangle$ are larger in the midsheath and near-LE regions than in the near-shock region. The bottom row in Figure 9 shows that the fast-ejecta sheaths lack high solar wind densities (i.e., values of $N_p > 20$ cm^{-3}). In turn, slow-ejecta sheaths are often dominated by $Np > 20$ cm^{-3} plasma. This occurs most frequently in the midsheath, where 44% of the cases have > 0.67 coverage of $Np > 20$ cm^{-3}. Furthermore, for the slow-ejecta sheaths, the midsheath and the near-LE regions lack $Np > 20$ cm^{-3} plasma in only 24% and 29% of the cases, respectively, while for the near-shock region this occurs for 43% of the cases. The strong and weak-ejecta sheaths show however much clearer variations (Figures 8f–8h). In particular,

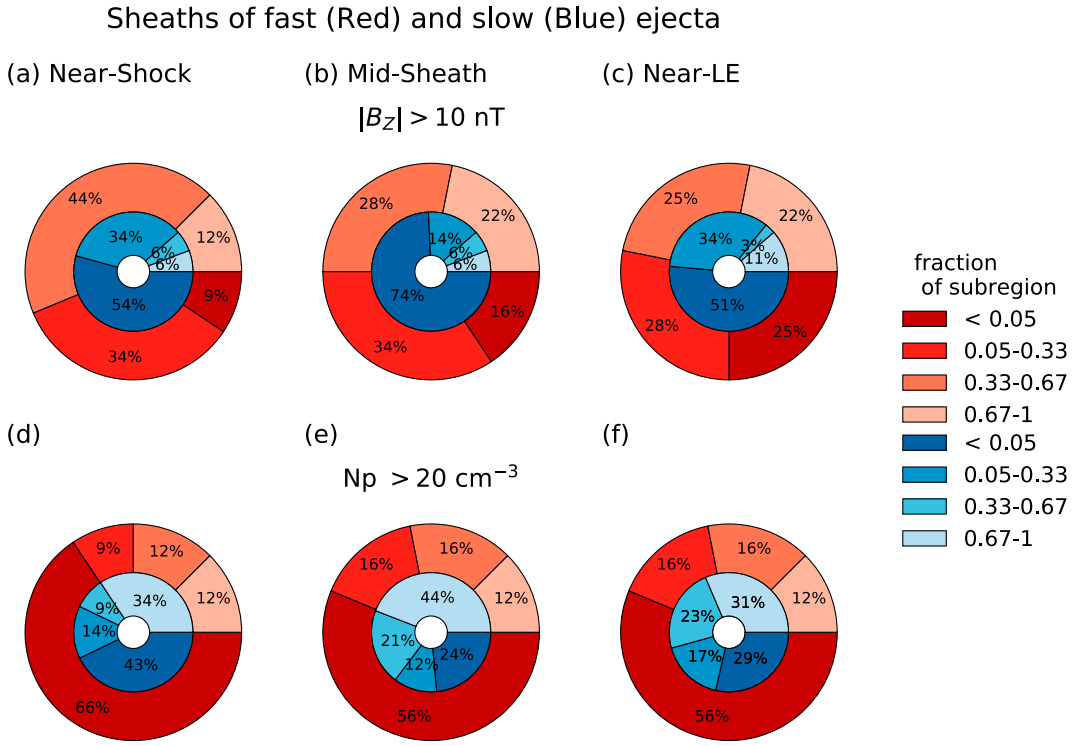

Figure 9. (top) The percentages of the cases showing different fractions of a sheath subregion occupied by strong out-of-ecliptic fields ($|B_Z| > 10$ nT). The outer red donut gives the percentages for the sheaths of fast (leading edge speed $V_{LE} > 550$ km/s) ejecta and the blue inner ring for the sheaths of slow ($V_{LE} < 550$ km/s) ejecta. (bottom) Same but for high densities ($N_p > 20$ cm^{-3}). LE = leading edge.

for the strong-ejecta sheaths, the median $\langle N_p \rangle$ decreases from the near-shock region to near-LE region, and the median $\langle P_{dyn} \rangle$ peaks in the midsheath region. The bottom row of Figure 10 shows that for the red subset, strong densities $N_p > 20$ cm^{-3} occupied the majority of the near-shock region in 52% of the cases. This was the case also for 44% of the midsheath regions, but only 26% for the near-LE region. The three subregions feature however similar percentages of cases with a negligible fraction of $N_p > 20$ cm^{-3} values. The distribution of relative occurrences for the > 0.66 incidences for $N_p > 20$ cm^{-3} are also shown in Table S2 in the supporting information. Now there are more events when incidences overlap, in particular for the strong-ejecta sheaths that have four events when > 0.66 incidence of $N_p > 20$ cm^{-3} occurs simultaneously in all three subregions and six cases when it occurs simultaneously in the near-shock and midsheath regions. For the slow-ejecta sheaths the > 0.66 incidence of $N_p > 20$ cm^{-3} occur typically either in one subregions only or simultaneously in the near-shock and midsheath regions.

Figures 7i and 8i show that the magnetopause can be compressed/eroded throughout the sheath, but the plots suggest that the strongest compression is typically found in the near-LE region. Similarly, the bottom rows in Figures 7 and 8 show that geomagnetic activity can also occur throughout the sheath. In all cases, the median $\langle SYM\text{-}H \rangle$ decreases from the near-shock region to the near-LE region, while the median PCN and *AL* show the least disturbed values in the midsheath region.

3.3. Correlation Between Ejecta and Sheath Parameters

Finally, we investigate how sheath parameters correlate with the ejecta leading edge speed (V_{LE}) and with the leading edge magnetic field (B_{LE}).

Figure 11 shows scatter plots of the average sheath parameters in different subregions (near-shock: dark purple, midsheath: medium purple, and near-LE: light purple) and the ejecta leading edge speed V_{LE}. Correlation coefficients (*cc*) are also shown in each panel. The figure reveals an almost perfect correlation ($cc \geq 0.92$) between V_{LE} and average speed $\langle V_p \rangle$ (Figure 11d) for all sheath subregions. Otherwise, only moderate ($cc = 0.7$–0.5), poor ($cc = 0.5$–0.3), or nonexistent ($cc < 0.3$) correlations are found. Sheath $\langle B \rangle$ (Figure 11a) and $\langle B_{RMS} \rangle$ (Figure 11c) show moderate correlation with V_{LE} in the near-shock region. For the

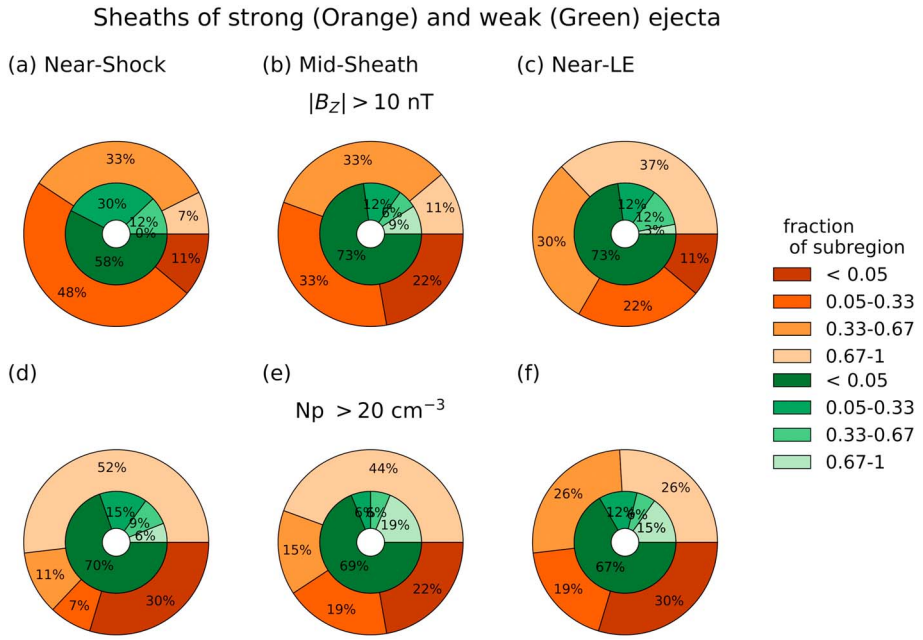

Figure 10. (top) The percentages of cases showing different fractions of a sheath subregion occupied by strong out-of-ecliptic fields ($|B_Z| > 10$ nT). The outer orange donut gives the percentages for the sheaths of strong (leading edge B field $B_{\rm LE} > 18$ nT) ejecta and the green inner ring for the sheaths of the slow ($B_{\rm LE} < 14$ nT) ejecta. (bottom) Same but for high densities ($N_p > 20$ cm^{-3}). LE = leading edge.

other two subregions correlations are poor or even nonexistent (in the case of sheath $\langle |B_Z| \rangle$ in the near-LE region). Sheath $< |E_Y| >$ (Figure 11e) shows moderate correlation with $V_{\rm LE}$ for all subregions. In turn, no linear relationship exists between $V_{\rm LE}$ and the sheath $\langle N_p \rangle$ (Figure 11f) or $\langle M_A \rangle$ (Figure 11h), and the correlations between $V_{\rm LE}$ and sheath $\langle P_{\rm dyn} \rangle$ (Figure 11g) and $< R_{\rm mp} >$ (Figure 11i) are poor. The highest correlations are found in the near-shock region, with $cc = 0.5$ and $cc = -0.46$ for $\langle P_{\rm dyn} \rangle$ and $< R_{\rm mp} >$, respectively. Correlation between $\langle SYM\text{-}H \rangle$ and $V_{\rm LE}$ (Figure 11j) is strongest for the near-LE region, while $\langle$PCN$\rangle$ and $\langle AL \rangle$ (Figures 11k and 11l) show moderate to poor correlation with $V_{\rm LE}$, the correlation being again highest in the near-shock region.

Correlations between different sheath parameters and the ejecta leading edge magnetic field magnitude $B_{\rm LE}$, Figure 12, are generally considerably lower than with $V_{\rm LE}$. The only strong correlation we found is between the magnetic field magnitude and $B_{\rm LE}$ (Figure 12a) in the near-LE region ($cc = 0.78$). Regarding sheath $|B_Z|$, $B_{\rm RMS}$, and $|E_Y|$ (Figures 12b, 12c, and 12e), correlation with $B_{\rm LE}$ is significant only in the near-LE region, showing moderate correlation. Otherwise, correlations are either poor or nonexistent.

4. Summary and Discussion

In this paper we have performed a comprehensive investigation of solar wind properties and geomagnetic indices in CME-driven sheath regions and their dependence on the properties of the driving ejecta. A special focus has been put on the variations in different parts of the sheath. Our study includes 89 sheath regions in the near-Earth solar wind during Solar Cycles 23 and 24 (from January 1997 to June 2018). We included only those cases that featured a clear transition from the sheath to the ejecta. Solar wind parameters and geomagnetic responses were investigated separately in three different sheath regions: near-shock, midsheath, and near-LE regions.

First, our results highlight a large range of values for IMF and solar wind parameters in sheaths; for example, their magnetic field magnitudes range from a few nanoteslas to about 50 nT, densities from a few per cubic centimeters to about 80 cm^{-3}, and speeds from less than 300 to over 1,000 km/s. The subsolar magnetopause position during the passage of sheaths is typically well below its nominal value ($\sim$ 10–12R_E), and for a significant fraction of time, pushed close to or even below the geostationary orbit (6.6R_E). The geomagnetic indices *SYM-H*, PCN, and *AL* range from quiet to highly disturbed values.

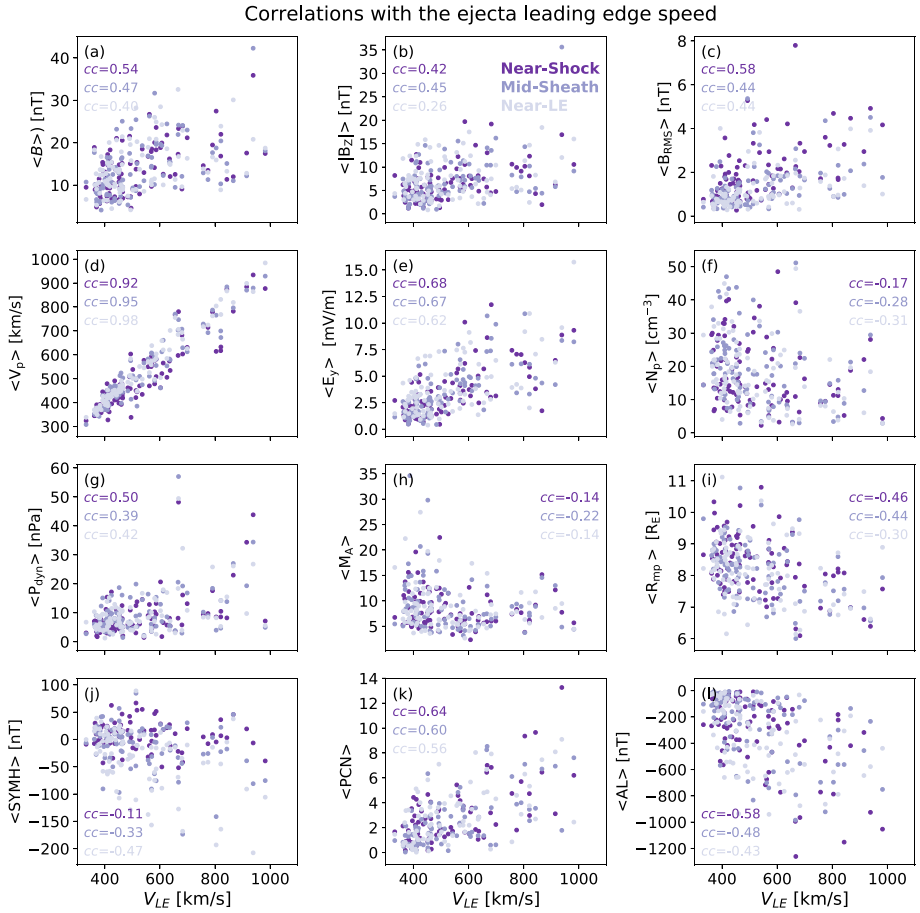

Figure 11. Correlation between the ejecta leading edge speed (V_{LE}) and the averages of the selected solar wind and geomagnetic parameters in three sheath subregions (near-shock: dark purple, midsheath: medium purple, near-LE: light purple). Correlation coefficients (*cc*) are shown in each panel. The panels are presented in the same format as in Figure 2. LE = leading edge.

By performing a statistical analysis of sheath regions spanning two solar cycles, our study confirms the previous findings discussed in section 1: CME-driven sheaths exhibit significantly more compressed plasma and fluctuating magnetic fields than the (undisturbed) solar wind ahead and the following ejecta. The Alfvén Mach number in sheaths is similar to that in the preceding solar wind but much higher than in the following ejecta. Sheaths also compress/erode the magnetosphere more efficiently than their corresponding ejecta. The finding that *SYM-H* was more disturbed on average in the ejecta, while *AL* and PCN have more similar levels in the sheath and the ejecta (although we note that only the first 5 hr of the leading part of the ejecta were included in this study) is consistent with Huttunen et al. (2002) and Huttunen and Koskinen (2004), suggesting that ejecta affect more the ring current, while sheaths are effective in causing strong variations of the auroral currents.

From the investigated ejecta properties, we found that only their speed (leading edge speed, expansion speed, and speed relative to the preceding solar wind) and magnetic field strength divided sheaths into distinct populations. Interestingly, we did not find any clear difference between centrally crossed FRs and complex ejecta (non-FRs), nor any dependence on the tilt of the FR or sheath thickness. The results, however, suggest that sheaths related to complex ejecta are slightly faster and more geoeffective (due to higher speeds) than sheaths preceding FR ejecta. Since the number of sheaths of complex ejecta was relatively small in this study, no strong conclusions can be drawn. Nevertheless, this is a topic that would be interesting to investigate in further detail in the future.

Our statistical analysis finds the fast ejecta to be most likely preceded by geoeffective sheaths; fast-ejecta sheaths have on average high solar wind speeds and magnetic fields and, consequently, intense driving

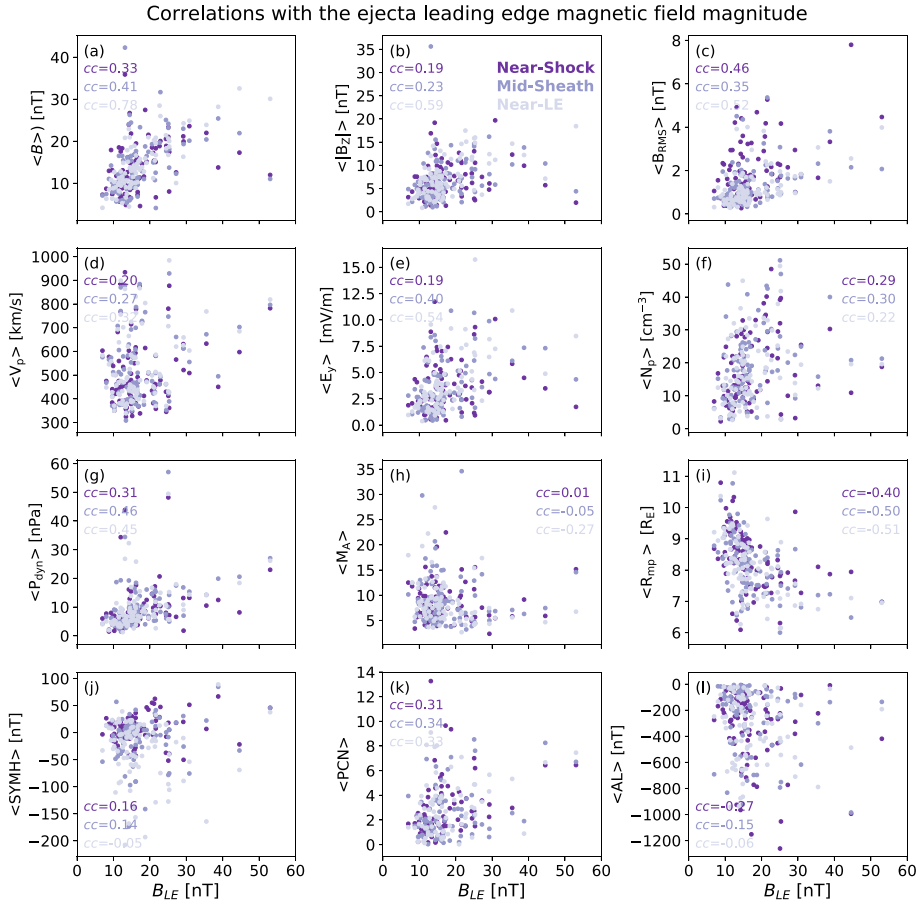

Figure 12. Correlation between the ejecta leading edge magnetic field magnitude (B_{LE}) and the averages of the selected solar wind parameters in three sheath subregions (near-shock: dark purple, midsheath: medium purple, near-LE: light purple). Correlation coefficients (*cc*) are shown in each panel. The panels are presented in the same format as in Figure 2. LE = leading edge.

electric fields. They also have strong magnetic field fluctuations, as estimated by OMNI root-mean-square 1-min measured field (B_{RMS}). This is consistent with Kilpua et al. (2013) who found that the ULF Pc5 range (from 3 to 10 min) fluctuation power was strong in sheaths associated with fast ejecta. The sheaths associated with the strong B field ejecta caused also a considerable amount of intense geomagnetic activity but clearly less than the sheaths preceding the fast ejecta. This was featured both by distributions for the whole data set, sheath frequency distribution as a function of their median, 90th percentile, and the coverage of moderate and intense geomagnetic activity in the sheath.) We found that fast and strong ejecta create almost equally effectively strong out-of-ecliptic fields in their sheaths; over one third of the data points had $|B_Z| > 10$ nT values for both of these subsets, although there was a strong variability in the coverage of $|B_Z| > 10$ nT from event to event. The lower average geoeffectiveness of the strong-ejecta sheaths is thus likely a consequence of their lower speeds and field fluctuations when compared to the fast-ejecta sheaths. When the sheaths were sorted according to the ejecta LE magnetic field strength, the sheaths of strong and weak ejecta had very similar speed distributions, with their median speeds considerably lower than for the fast-ejecta sheaths. We however note that the strong-ejecta sheaths had a tendency for higher solar wind densities and dynamic pressure that can enhance their coupling with the magnetosphere (e.g., Kilpua, Balogh et al., 2017). The sheaths preceding the slow and weak ejecta caused mainly moderate level geomagnetic activity. We found that such sheaths have relatively high Alfvén Mach numbers, and although they rarely embed strongly out-of-ecliptic fields, they frequently have a significant coverage of moderately ($|B_Z| > 5$ nT) out-of-ecliptic fields. This was the case in particular for the slow-ejecta sheaths that were also characterized by high densities and relatively high dynamic pressure.

The tendency of slow-ejecta sheaths to have strong densities is interesting. It is possible that large densities are related to some preferred source region at the Sun affecting the solar wind conditions that slow CMEs encounter ahead and/or because it takes more time for slow CMEs to propagate from Sun to Earth. It is known that slow CMEs originate more often close to the streamer belt; that is, they represent streamer blow-out CMEs or are related to quiescent filament eruptions, while fast CMEs mostly come from active regions (e.g., Sheeley et al., 1999). Table S3 in the supporting information gives the median values of the IMF magnitude, $|B_Z|$, B_{RMS}, solar wind speed, and density over 5-hr interval preceding the fast-, slow-, strong-, and weak-ejecta sheaths. The median densities of the preceding solar wind for the slow- and fast-ejecta sheaths are 5.4 and 7.6 cm^{-3}, respectively; that is, the slow-ejecta sheaths investigated here were preceded by a somewhat higher (41%) densities than the fast-ejecta sheaths. This could imply that slow CMEs interact more frequently with high-density solar wind structures, such as the heliospheric plasma sheet. The strong-ejecta sheaths had also a tendency for high densities and as shown by Table S3 they were preceded by the solar wind with similar median density as the slow-ejecta sheaths. The strong-ejecta sheaths that had the highest densities were also associated with the slowest ejecta in the subset: If we use the median density of 20 cm^{-3} as the threshold between high-density and low-density sheaths in the strong-ejecta sheath subset, the median ejecta speed for the high-density sheaths is 503 km/s and for the low-density sheaths 638 km/s. Janvier et al. (2019) also noted that weak sheaths were preceded by weaker IMF magnitude than strong sheaths, and they suggest also that this characteristic could stem from the properties of the source region of the CMEs. In agreement with our data set (see Table S3) weak- and also slow-ejecta sheaths are preceded by weaker IMF than the fast- and in particular strong-ejecta sheaths. This could imply that the tendency of the fast- and strong-ejecta sheaths to have strong fields partly stems from the strong preceding IMF that is processed further by the shock and getting draped around the ejecta. We also note that the fast- and strong-ejecta sheaths are preceded by solar wind featuring higher fluctuations and the fast-ejecta sheaths are preceded by the faster solar wind than other investigated subsets. These findings imply that the preceding solar wind plays and important role in dictating sheath properties.

The fast- and strong-ejecta sheaths compress/erode the most effectively the dayside magnetopause. We found that for these subsets the majority of events compressed the magnetopause significantly, beyond $< 8R_E$, and typically this occurred at least 50% time of the sheath duration, while clearly a smaller fraction of events led to a compression beyond geostationary orbit, and it occurred typically only for relatively short fraction of sheath duration. We however note that even a relatively short period of compression beyond or close to geostationary orbit can empty quickly in particular the outer parts of the outer Van Allen radiation belts (e.g., Kilpua et al., 2019). As the fast- and strong-ejecta sheaths have also typically strong magnetic field fluctuations, high dyn pessure, and moderate to intense ring current response, they are expected to cause particularly strong and deep losses of relativistic electrons from the outer radiation belt due to effective magnetopause shadowing (Hietala et al., 2014; Kilpua, Hietala, et al., 2015; Kilpua et al., 2019; Turner et al., 2019). Our study also suggests that sheaths of slow ejecta can also compress/erode the subsolar magnetopause significantly, but very rarely beyond the geostationary orbit and also compression/erosion beyond $< 8R_E$ occurs typically less than 50% of the sheath duration.

We also found some clear trends in how solar wind parameters and geospace response vary across the sheath, from the shock to the ejecta LE. One of the clearest trends was for the magnetic field fluctuations that peaked close to the shock for all investigated subsets; in particular this trend was distinct for the sheaths of fast ejecta. This suggests that for fast-ejecta shock processes (field compression and alignment of discontinuities; e.g., Kataoka, Watari et al., 2005; Palmerio et al., 2016) effectively enhance fluctuations downstream of the shock. We note that we investigated here only 1-min-range fluctuations, while as discussed in section 1, there is a wider range of possible fluctuations that affect solar wind-magnetosphere coupling and consequently to sheath geoeffectiveness. It would be an interesting future study to investigate these fluctuations more comprehensively, both how they relate to shock and driving CME properties and geomagnetic activity.

The magnetic field magnitude and $|B_Z|$ were however more stable across the sheath for fast ejecta, suggesting that both shock processes and field line draping play an important role in creating out-of-ecliptic fields (see, e.g., discussion in Palmerio et al., 2016). In strong-ejecta sheaths, B field magnitude and $|B_Z|$ in turn peak close to the ejecta LE, suggesting the importance of field draping processes. We further found that the solar wind density peaks in the midsheath and near-LE regions for weak-ejecta sheaths, but close to the shock for strong-ejecta sheaths. For the sheaths of fast and slow ejecta, densities were more stable throughout the sheath. We emphasize that sheaths can compress/erode the magnetopause inward and be geoeffective

throughout their duration. We however found that the most geoeffective part of the sheath in terms of *SYM-H* is the near-LE region as *SYM-H* takes time to develop, while *AL* peaked in both the near-shock and near-LE regions. The compression of the magnetosphere is the most likely close to the ejecta LE.

Consistently with Mitsakou et al. (2009) and Janvier et al. (2019; both of which studied the sheath as a single entity), we found a strong correlation between the ejecta LE speed and the speed in the sheath. We further demonstrated that this high correlations exists throughout the sheath by investigating correlations separately for three sheath subregions. We also found a significant correlation between the ejecta LE speed and the solar wind driving electric field in the sheath for all subregions. The relations between the ejecta LE speed and the sheath magnetic field characteristics were on the other hand only from moderate to poor, the highest correlations occurring close to the shock. Janvier et al. (2019) also reported a tendency that fast-ejecta sheaths have higher magnetic field magnitudes than slow ejecta (correlation coefficient 0.54), which they connected to the shock compression and higher dynamic pressure from behind due to the driving ejecta. In particular, fluctuations in the sheath increase with increasing ejecta speed and correlations are highest in the near-shock region. As discussed in section 1, Owens et al. (2005) reported no relationship between the mean field strength in sheaths and the ejecta speed, except for the magnetic cloud subset. The correlations between the ejecta LE magnetic field strength and the sheath parameters were generally much lower. Significant correlations exist only in the near-LE region for sheath magnetic parameters. We found no relationship between the ejecta LE speed/field strength and the solar wind density and Alfvén Mach number in any of the sheath subregions.

To conclude, our study highlights that CME-driven sheaths are highly relevant structures from the space weather point of view that effectively cause moderate to intense activity and compress strongly the magnetosphere for a substantial fraction of time during their passage at Earth. This study also highlights the variable and complex nature of sheaths, but nevertheless finds some clear trends that could be useful to predict their space weather responses. The most significant geoeffects are expected from the sheaths driven by fast CMEs, although we note that slow-ejecta sheaths can cause frequently moderate activity. Sheaths associated with weak *B* field ejecta are the least geoeffective in terms of causing geomagnetic disturbances and compressing the magnetosphere. The most geoeffective parts within the sheath are the near-shock and near-LE regions. There is currently no practical method to forecast field and plasma parameters in sheaths. It is also questionable to what extent current magnetohydrodynamic heliospheric simulations (e.g., Odstrcil, 2003; Pomoell & Poedts, 2018) and analytic models (e.g., Romashets et al., 2008) can predict sheath properties. A more complete understanding of statistical variations of space weather relevant parameters in sheaths and their dependencies on driver properties could help to estimate their consequences using remote-sensing observations of CMEs.

Acknowledgments
E. K. acknowledges the European Research Council (ERC) under the European Union's Horizon 2020 research and innovation programme project SolMAG 724391 and Academy of Finland project 1267087. E. Y. was supported by the Swedish Civil Contingencies Agency, Grant 2016-2102. M. P. is covered by ERC Grant 682068-PRESTISSIMO. The results presented in here have been achieved under the framework of the Finnish Centre of Excellence in Research of Sustainable Space (Academy of Finland Grant 1312390), which we gratefully acknowledge. This work has been done within the LABEX Plas@par project and received financial state aid managed by the Agence Nationale de laRecherche, as part of the programme "Investissements d'avenir" under the reference ANR-11-IDEX-0004-02. D. F. acknowledges the project TEMPETE (ANR-17-CE31-0016-02) funded by the Agence Nationale de la Recherche. This paper uses 1-min OMNI data accessed through NASA/GSFC's Space Physics Data Facility's CDAWeb service (https://cdaweb.sci.gsfc.nasa.gov/), which we gratefully acknowledge.

References

Alves, L. R., Da Silva, L. A., Souza, V. M., Sibeck, D. G., Jauer, P. R., Vieira, L. E. A., et al. (2016). Outer radiation belt dropout dynamics following the arrival of two interplanetary coronal mass ejections. *Geophysical Research Letters*, *43*, 978–987. https://doi.org/10.1002/2015GL067066

Borovsky, J. E., & Funsten, H. O. (2003). Role of solar wind turbulence in the coupling of the solar wind to the Earth's magnetosphere. *Journal of Geophysical Research*, *108*, 1246. https://doi.org/10.1029/2002JA009601

Bothmer, V., & Schwenn, R. (1998). The structure and origin of magnetic clouds in the solar wind. *Annales Geophysicae*, *16*, 1–24. https://doi.org/10.1007/s00585-997-0001-x

Burlaga, L. F. (1988). Magnetic clouds and force-free fields with constant alpha. *Journal of Geophysical Research*, *93*, 7217–7224. https://doi.org/10.1029/JA093iA07p07217

Burlaga, L., Sittler, E., Mariani, F., & Schwenn, R. (1981). Magnetic loop behind an interplanetary shock—Voyager, Helios, and IMP 8 observations. *Journal of Geophysical Research*, *86*, 6673–6684. https://doi.org/10.1029/JA086iA08p06673

Cane, H. V., & Richardson, I. G. (2003). Interplanetary coronal mass ejections in the near-Earth solar wind during 1996–2002. *Journal of Geophysical Research*, *108*(A4), 1156. https://doi.org/10.1029/2002JA009817

Cane, H. V., Richardson, I. G., & Wibberenz, G. (1997). Helios 1 and 2 observations of particle decreases, ejecta, and magnetic clouds. *Journal of Geophysical Research*, *102*, 7075–7086. https://doi.org/10.1029/97JA00149

Carley, E. P., Vilmer, N., Simões, P. J. A., & Ó Fearraigh, B. (2017). Estimation of a coronal mass ejection magnetic field strength using radio observations of gyrosynchrotron radiation. *Astronomy & Astrophysics*, *608*, A137. https://doi.org/10.1051/0004-6361/201731368

Elkington, S. R., Hudson, M. K., & Chan, A. A. (2003). Resonant acceleration and diffusion of outer zone electrons in an asymmetric geomagnetic field. *Journal of Geophysical Research*, *108*(A3), 1116. https://doi.org/10.1029/2001JA009202

Gonzalez, WalterD., Echer, Ezequiel, Tsurutani, BruceT., Clúa de Gonzalez, AliciaL., & Dal Lago, Alisson (2011). Interplanetary origin of intense, superintense and extreme geomagnetic storms. *Space Science Reviews*, *158*, 69–89. https://doi.org/10.1007/s11214-010-9715-2

Gonzalez, W. D., Joselyn, J. A., Kamide, Y., Kroehl, H. W., Rostoker, G., Tsurutani, B. T., & Vasyliunas, V. M. (1994). What is a geomagnetic storm? *Journal of Geophysical Research*, *99*, 5771–5792. https://doi.org/10.1029/93JA02867

Gosling, J. T., & McComas, D. J. (1987). Field line draping about fast coronal mass ejecta—A source of strong out-of-the-ecliptic interplanetary magnetic fields. *Geophysical Research Letters*, *14*, 355–358. https://doi.org/10.1029/GL014i004p00355

Gosling, J. T., McComas, D. J., Phillips, J. L., & Bame, S. J. (1991). Geomagnetic activity associated with Earth passage of interplanetary shock disturbances and coronal mass ejections. *Journal of Geophysical Research*, *96*, 7831–7839. https://doi.org/10.1029/91JA00316

Green, L. M., Török, T., Vršnak, B., Manchester, W., & Veronig, A. (2018). The origin, early evolution and predictability of solar eruptions. *Space Science Reviews*, *214*, 46. https://doi.org/10.1007/s11214-017-0462-5

Guo, J., Feng, X., Zhang, J., Zuo, P., & Xiang, C. (2010). Statistical properties and geoefficiency of interplanetary coronal mass ejections and their sheaths during intense geomagnetic storms. *Journal of Geophysical Research*, *115*, A09107. https://doi.org/10.1029/2009JA015140

Hajra, R., & Tsurutani, B. T. (2018). Interplanetary shocks inducing magnetospheric supersubstorms (SML ≤ -2500 nT): Unusual auroral morphologies and energy flow. *The Astrophysical Journal*, *858*, 123. https://doi.org/10.3847/1538-4357/aabaed

Hietala, H., Kilpua, E. K. J., Turner, D. L., & Angelopoulos, V. (2014). Depleting effects of ICME-driven sheath regions on the outer electron radiation belt. *Geophysical Research Letters*, *41*, 2258–2265. https://doi.org/10.1002/2014GL059551

Huttunen, K. E. J., Kilpua, S. P., Pulkkinen, A., Viljanen, A., & Tanskanen, E. (2008). Solar wind drivers of large geomagnetically induced currents during the Solar Cycle 23. *Space Weather*, *6*, S10002. https://doi.org/10.1029/2007SW000374

Huttunen, K., & Koskinen, H. (2004). Importance of post-shock streams and sheath region as drivers of intense magnetospheric storms and high-latitude activity. *Annales Geophysicae*, *22*, 1729–1738. https://doi.org/10.5194/angeo-22-1729-2004

Huttunen, K. E. J., Koskinen, H. E. J., & Schwenn, R. (2002). Variability of magnetospheric storms driven by different solar wind perturbations. *Journal of Geophysical Research*, *107*(A7), 1121. https://doi.org/10.1029/2001JA900171

Huttunen, K. E. J., Schwenn, R., Bothmer, V., & Koskinen, H. E. J. (2005). Properties and geoeffectiveness of magnetic clouds in the rising, maximum and early declining phases of Solar Cycle 23. *Annales Geophysicae*, *23*, 625–641. https://doi.org/10.5194/angeo-23-625-2005

Janvier, M., Winslow, R. M., Good, S., Bonhomme, E., Démoulin, P., Dasso, S., et al. (2019). Generic magnetic field intensity profiles of interplanetary coronal mass ejections at Mercury, Venus, and Earth from superposed epoch analyses. *Journal of Geophysical Research: Space Physics*, *124*, 812–836. https://doi.org/10.1029/2018JA025949

Jian, L., Russell, C. T., Luhmann, J. G., & Skoug, R. M. (2006). Properties of interplanetary coronal mass ejections at one AU during 1995–2004. *Solar Physics*, *239*, 393–436. https://doi.org/10.1007/s11207-006-0133-2

Kataoka, R., Fairfield, D. H., Sibeck, D. G., Rastätter, L., Fok, M.-C., Nagatsuma, T., & Ebihara, Y. (2005). Magnetosheath variations during the storm main phase on 20 November 2003: Evidence for solar wind density control of energy transfer to the magnetosphere. *Geophysical Research Letters*, *32*, L21108. https://doi.org/10.1029/2005GL022777

Kataoka, R., & Miyoshi, Y. (2006). Flux enhancement of radiation belt electrons during geomagnetic storms driven by coronal mass ejections and corotating interaction regions. *Space Weather*, *4*, 09004. https://doi.org/10.1029/2005SW000211

Kataoka, R., Shiota, D., Kilpua, E., & Keika, K. (2015). Pileup accident hypothesis of magnetic storm on 17 March 2015. *Geophysical Research Letters*, *42*, 5155–5161. https://doi.org/10.1002/2015GL064816

Kataoka, R., Watari, S., Shimada, N., Shimazu, H., & Marubashi, K. (2005). Downstream structures of interplanetary fast shocks associated with coronal mass ejections. *Geophysical Research Letters*, *32*, L12103. https://doi.org/10.1029/2005GL024495

Kaymaz, Z., & Siscoe, G. (2006). Field-line draping around ICMES. *Solar Physics*, *239*, 437–448. https://doi.org/10.1007/s11207-006-0308-x

Kessel, R., Mann, I., Fung, S., Milling, D., & O'Connell, N. (2004). Correlation of Pc5 wave power inside and outside the magnetosphere during high speed streams. *Annales Geophysicae*, *22*, 629–641. https://doi.org/10.5194/angeo-22-629-2004

Kilpua, E. K. J., Balogh, A., von Steiger, R., & Liu, Y. D. (2017). Geoeffective properties of solar transients and stream interaction regions. *Space Science Reviews*, *212*, 1271–1314. https://doi.org/10.1016/j.jastp.2010.10.012

Kilpua, E. K. J., Hietala, H., Koskinen, H. E. J., Fontaine, D., & Turc, L. (2013). Magnetic field and dynamic pressure ULF fluctuations in coronal-mass-ejection-driven sheath regions. *Annales Geophysicae*, *31*, 1559–1567. https://doi.org/10.5194/angeo-31-1559-2013

Kilpua, E. K. J., Hietala, H., Turner, D. L., Koskinen, H. E. J., Pulkkinen, T. I., Rodriguez, J. V., et al. (2015). Unraveling the drivers of the storm time radiation belt response. *Geophysical Research Letters*, *42*, 3076–3084. https://doi.org/10.1002/2015GL063542

Kilpua, E. K. J., Jian, L. K., Li, Y., Luhmann, J. G., & Russell, C. T. (2011). Multipoint ICME encounters: Pre-STEREO and STEREO observations. *Journal of Atmospheric and Solar-Terrestrial Physics*, *73*, 1228–1241. https://doi.org/10.1016/j.jastp.2010.10.012

Kilpua, E., Koskinen, H. E. J., & Pulkkinen, T. I. (2017). Coronal mass ejections and their sheath regions in interplanetary space. *Living Reviews in Solar Physics*, *14*, 5. https://doi.org/10.1007/s41116-017-0009-6

Kilpua, E. K. J., Lumme, E., Andreeova, K., Isavnin, A., & Koskinen, H. E. J. (2015). Properties and drivers of fast interplanetary shocks near the orbit of the Earth (1995–2013). *Journal of Geophysical Research: Space Physics*, *120*, 4112–4125. https://doi.org/10.1002/2015JA021138

Kilpua, E. K. J., Turner, D. L., Jaynes, A. N., Hietala, H., Koskinen, H. E. J., Osmane, A., et al. (2019). Outer Van Allen radiation belt response to interacting interplanetary coronal mass ejections. *Journal of Geophysical Research: Space Physics*, *124*, 1927–1947. https://doi.org/10.1029/2018JA026238

Klein, L. W., & Burlaga, L. F. (1982). Interplanetary magnetic clouds at 1 AU. *Journal of Geophysical Research*, *87*, 613–624. https://doi.org/10.1029/JA087iA02p00613

Knipp, D., Kilcommons, L., Hunt, L., Mlynczak, M., Pilipenko, V., Bowman, B., et al. (2013). Thermospheric damping response to sheath-enhanced geospace storms. *Geophysical Research Letters*, *40*, 1263–1267. https://doi.org/10.1002/grl.50197

Knipp, D. J., Pette, D. V., Kilcommons, L. M., Isaacs, T. L., Cruz, A. A., Mlynczak, M. G., et al. (2017). Thermospheric nitric oxide response to shock-led storms. *Space Weather*, *15*, 325–342. https://doi.org/10.1002/2016SW001567

Lopez, R. E., Wiltberger, M., Hernandez, S., & Lyon, J. G. (2004). Solar wind density control of energy transfer to the magnetosphere. *Geophysical Research Letters*, *31*, L08804. https://doi.org/10.1029/2003GL018780

Lugaz, N., Farrugia, C. J., Winslow, R. M., Al-Haddad, N., Kilpua, E. K. J., & Riley, P. (2016). Factors affecting the geoeffectiveness of shocks and sheaths at 1 AU. *Journal of Geophysical Research: Space Physics*, *121*, 10,861–10,879. https://doi.org/10.1002/2016JA023100

Mayaud, P. N. (1980). *Derivation, meaning, and use of geomagnetic indices*, Geophysical Monograph (Vol. 22). Washington, DC: American Geophysical Union.

McComas, D. J., Gosling, J. T., Winterhalter, D., & Smith, E. J. (1988). Interplanetary magnetic field draping about fast coronal mass ejecta in the outer heliosphere. *Journal of Geophysical Research*, *93*, 2519–2526. https://doi.org/10.1029/JA093iA04p02519

Mierla, M., Inhester, B., Antunes, A., Boursier, Y., Byrne, J. P., Colaninno, R., et al. (2010). On the 3-D reconstruction of coronal mass ejections using coronagraph data. *Annales Geophysicae*, *28*, 203–215. https://doi.org/10.5194/angeo-28-203-2010

Mitsakou, E., Babasidis, G., & Moussas, X. (2009). Interplanetary coronal mass ejections during the descending cycle 23: Sheath and ejecta properties comparison. *Advances in Space Research*, *43*, 495–498. https://doi.org/10.1016/j.asr.2008.08.003

Mulligan, T., Russell, C. T., & Luhmann, J. G. (1998). Solar cycle evolution of the structure of magnetic clouds in the inner heliosphere. *Geophysical Research Letters*, *25*, 2959–2962. https://doi.org/10.1029/98GL01302

Myllys, M., Kilpua, E. K. J., Lavraud, B., & Pulkkinen, T. I. (2016). Solar wind-magnetosphere coupling efficiency during ejecta and sheath-driven geomagnetic storms. *Journal of Geophysical Research: Space Physics*, *121*, 4378–4396. https://doi.org/10.1002/2016JA022407

Nieves-Chinchilla, T., Linton, M. G., Hidalgo, M. A., Vourlidas, A., Savani, N. P., Szabo, A., et al. (2016). A circular-cylindrical flux-rope analytical model for magnetic clouds. *The Astrophysical Journal*, *823*, 27. https://doi.org/10.3847/0004-637X/823/1/27

Nieves-Chinchilla, T., Vourlidas, A., Raymond, J. C., Linton, M. G., Al-haddad, N., Savani, N. P., et al. (2018). Understanding the internal magnetic field configurations of ICMES using more than 20 years of wind observations. *Solar Physics*, *293*, 25. https://doi.org/10.1007/s11207-018-1247-z

Nykyri, K., & Dimmock, A. P. (2016). Statistical study of the ULF Pc4–Pc5 range fluctuations in the vicinity of Earth's magnetopause and correlation with the low latitude boundary layer thickness. *Advances in Space Research*, *58*, 257–267. https://doi.org/10.1016/j.asr.2015.12.046

Odstrcil, D. (2003). Modeling 3-D solar wind structure. *Advances in Space Research*, *32*, 497–506. https://doi.org/10.1016/S0273-1177(03)00332-6

Osmane, A., Dimmock, A. P., Naderpour, R., Pulkkinen, T. I., & Nykyri, K. (2015). The impact of solar wind ULF B_z fluctuations on geomagnetic activity for viscous timescales during strongly northward and southward IMF. *Journal of Geophysical Research: Space Physics*, *120*, 9307–9322. https://doi.org/10.1002/2015JA021505

Owens, M. J., Cargill, P. J., Pagel, C., Siscoe, G. L., & Crooker, N. U. (2005). Characteristic magnetic field and speed properties of interplanetary coronal mass ejections and their sheath regions. *Journal of Geophysical Research*, *110*, A01105. https://doi.org/10.1029/2004JA010814

Owens, M. J., Lockwood, M., & Barnard, L. A. (2017). Coronal mass ejections are not coherent magnetohydrodynamic structures. *Scientific Reports*, *7*, 4152. https://doi.org/10.1038/s41598-017-04546-3

Palmerio, E., Kilpua, E. K. J., & Savani, N. P. (2016). Planar magnetic structures in coronal mass ejection-driven sheath regions. *Annales Geophysicae*, *34*, 313–322. https://doi.org/10.5194/angeo-34-313-2016

Pomoell, J., & Poedts, S. (2018). EUHFORIA: European heliospheric forecasting information asset. *Journal of Space Weather and Space Climate*, *8*(27), A35. https://doi.org/10.1051/swsc/2018020

Richardson, I. G., & Cane, H. V. (1995). Regions of abnormally low proton temperature in the solar wind (1965–1991) and their association with ejecta. *Journal of Geophysical Research*, *100*, 23,397–23,412. https://doi.org/10.1029/95JA02684

Richardson, I. G., & Cane, H. V. (2010). Near-Earth interplanetary coronal mass ejections during Solar Cycle 23 (1996–2009): Catalog and summary of properties. *Solar Physics*, *264*, 189–237. https://doi.org/10.1007/s11207-010-9568-6

Richardson, I. G., & Cane, H. V. (2012). Solar wind drivers of geomagnetic storms during more than four solar cycles. *Journal of Space Weather and Space Climate*, *2*(27), A01. https://doi.org/10.1051/swsc/2012001

Richardson, J. D., Liu, Y., Wang, C., & Burlaga, L. F. (2006). ICMEs at very large distances. *Advances in Space Research*, *38*, 528–534. https://doi.org/10.1016/j.asr.2005.06.049

Rodriguez, L., Masías-Meza, J. J., Dasso, S., Démoulin, P., Zhukov, A. N., Gulisano, A. M., et al. (2016). Typical profiles and distributions of plasma and magnetic field parameters in magnetic clouds at 1 AU. *Solar Physics*, *291*, 2145–2163. https://doi.org/10.1007/s11207-016-0955-5

Romashets, E., Vandas, M., & Poedts, S. (2008). Magnetic field disturbances in the sheath region of a super-sonic interplanetary magnetic cloud. *Annales Geophysicae*, *26*, 3153–3158. https://doi.org/10.5194/angeo-26-3153-2008

Sheeley, N. R., Walters, J. H., Wang, Y.-M., & Howard, R. A. (1999). Continuous tracking of coronal outflows: Two kinds of coronal mass ejections. *Journal of Geophysical Research*, *104*, 24,739–24,768. https://doi.org/10.1029/1999JA900308

Shue, J.-H., Song, P., Russell, C. T., Steinberg, J. T., Chao, J. K., Zastenker, G., et al. (1998). Magnetopause location under extreme solar wind conditions. *Journal of Geophysical Research*, *103*, 17,691–17,700. https://doi.org/10.1029/98JA01103

Siscoe, G., MacNeice, P. J., & Odstrcil, D. (2007). East-west asymmetry in coronal mass ejection geoeffectiveness. *Space Weather*, *5*, S04002. https://doi.org/10.1029/2006SW000286

Stauning, P. (2013). The Polar Cap index: A critical review of methods and a new approach. *Journal of Geophysical Research: Space Physics*, *118*, 5021–5038. https://doi.org/10.1002/jgra.50462

Storch, H., & Zwiers, F. W. (1999). *Statistical analysis in climate research*. Cambridge: Cambridge University Press,

Thernisien, A., Vourlidas, A., & Howard, R. A. (2009). Forward modeling of coronal mass ejections using STEREO/SECCHI data. *Solar Physics*, *256*, 111–130. https://doi.org/10.1007/s11207-009-9346-5

Tsurutani, B. T., Hajra, R., Echer, E., & Gjerloev, J. W. (2015). Extremely intense (SML ≤ -2500 nT) substorms: Isolated events that are externally triggered? *Annales Geophysicae*, *33*, 519–524. https://doi.org/10.5194/angeo-33-519-2015

Tsurutani, B. T., Smith, E. J., Gonzalez, W. D., Tang, F., & Akasofu, S. I. (1988). Origin of interplanetary southward magnetic fields responsible for major magnetic storms near solar maximum (1978–1979). *Journal of Geophysical Research*, *93*, 8519–8531. https://doi.org/10.1029/JA093iA08p08519

Tun, S. D., & Vourlidas, A. (2013). Derivation of the magnetic field in a coronal mass ejection core via multi-frequency radio imaging. *The Astrophysical Journal*, *766*, 130. https://doi.org/10.1088/0004-637X/766/2/130

Turner, D. L., Kilpua, E. K. J., Hietala, H., Claudepierre, S. G., O'Brien, T. P., Fennell, J. F., et al. (2019). The response of Earth's electron radiation belts to geomagnetic storms: Statistics from the Van Allen Probes era including effects from different storm drivers. *Journal of Geophysical Research: Space Physics*, *124*, 1013–1034. https://doi.org/10.1029/2018JA026066

Vorobjev, V. G., Antonova, E. E., & Yagodkina, O. I. (2018). How the intensity of isolated substorms is controlled by the solar wind parameters. *Earth, Planets and Space*, *70*, 148. https://doi.org/10.1186/s40623-018-0922-5

Vourlidas, A., Balmaceda, L. A., Stenborg, G., & Dal Lago, A. (2017). Multi-viewpoint coronal mass ejection catalog based on STEREO COR2 observations. *The Astrophysical Journal*, *838*, 141. https://doi.org/10.1007/s11207-012-0084-8

Vourlidas, A., Lynch, B. J., Howard, R. A., & Li, Y. (2013). How many CMEs have flux ropes? Deciphering the signatures of shocks, flux ropes, and prominences in coronagraph observations of CMEs. *Solar Physics*, *284*, 179–201. https://doi.org/10.3847/1538-4357/aa67f0

Webb, D. F., & Howard, T. A. (2012). Coronal mass ejections: Observations. *Living Reviews in Solar Physics*, *9*(3). https://doi.org/10.1007/lrsp-2012-3

Wei, F., Liu, R., Fan, Q., & Feng, X. (2003). Identification of the magnetic cloud boundary layers. *Journal of Geophysical Research*, *108*, 1263. https://doi.org/10.1007/lrsp-2012-3

Wei, F., Liu, R., Feng, X., Zhong, D., & Yang, F. (2003). Magnetic structures inside boundary layers of magnetic clouds. *Geophysical Research Letters*, *30*(24), 2283. https://doi.org/10.1029/2003GL018116

Yashiro, S., Gopalswamy, N., Michalek, G., St. Cyr, O. C., Plunkett, S. P., Rich, N. B., & Howard, R. A. (2004). A catalog of white light coronal mass ejections observed by the SOHO spacecraft. *Journal of Geophysical Research*, *109*, A07105. https://doi.org/10.1029/2003JA010282

Zhang, J., Richardson, I. G., Webb, D. F., Gopalswamy, N., Huttunen, E., Kasper, J. C., et al. (2007). Solar and interplanetary sources of major geomagnetic storms ($Dst \leq -100$ nT) during 1996–2005. *Journal of Geophysical Research*, *112*, A10102. https://doi.org/10.1029/2007JA012321

Zhou, X.-Y., Strangeway, R. J., Anderson, P. C., Sibeck, D. G., Tsurutani, B. T., Haerendel, G., et al. (2003). Shock aurora: FAST and DMSP observations. *Journal of Geophysical Research*, *108*(A4), 8019. https://doi.org/10.1029/2002JA009701

Zurbuchen, T. H., & Richardson, I. G. (2006). In-situ solar wind and magnetic field signatures of interplanetary coronal mass ejections. *Space Science Reviews*, *123*, 31–43. https://doi.org/10.1007/s11214-006-9010-4